Large-eddy simulations of a turbulent jet impinging on a vibrating heated wall

Natarajan, T, Jewkes, J, Lucey, AD, Narayanaswamy, R & Chung, YM

Original citation & hyperlink:
Natarajan, T, Jewkes, J, Lucey, AD, Narayanaswamy, R & Chung, YM 2017, 'Large-eddy simulations of a turbulent jet impinging on a vibrating heated wall' *International Journal of Heat and Fluid Flow*, vol 65, pp. 277-298
https://dx.doi.org/10.1016/j.ijheatfluidflow.2016.11.006

DOI 10.1016/j.ijheatfluidflow.2016.11.006
ISSN 0142-727X

Publisher: Elsevier

Large-eddy simulations of a turbulent jet impinging on a vibrating heated wall

Thangam Natarajan[†], James W. Jewkes[‡], Anthony D. Lucey[†], Ramesh Narayanaswamy[†1] and Yongmann M. Chung[*]

[†] Fluid Dynamics Research Group, Department of Mechanical Engineering, Curtin University, GPO Box U1987, Perth, WA 6845, Australia.

[‡] School of Mechanical, Aerospace and Automotive Engineering, Coventry University, Priory St, Coventry CV1 5FB, U.K.

[*] School of Engineering and Centre for Scientific Computing, University of Warwick Coventry CV4 7AL, U.K.

High-resolution large-eddy simulations (LES) are performed for an incompressible turbulent circular jet impinging upon a vibrating heated wall supplied with a constant heat flux. The present work serves to understand the flow dynamics and thermal characteristics of a turbulent jet under highly dynamic flow and geometric conditions. The baseline circular vibrating-wall jet impingement configuration undergoes a forced vibration in the wall-normal direction at the frequency, $f = 100\,\mathrm{Hz}$. The jet Reynolds number is $Re = DV_b/\nu = 23\,000$ and the nozzle-exit is at $y/D = 2$ where the wall vibrates between 0 and $0.5D$ with amplitude of vibration, $A = 0.25D$. The configuration is assembled through validation of sub-systems, in particular the method for generating the turbulent jet inflow and the baseline circular jet impingement configuration. Both time-mean and phase-averaged results are presented. The mean radial velocity increases upon positive displacement of the wall and decreases upon negative displacement but this correlation changes with increased radial distance from the stagnation point. Vortical structures are shown to play a major role in convective heat transfer even under the vibrating conditions of the impingement wall. Periodic shifts in the secondary Nusselt number peak are observed that depend upon the travelling eddy location and strength of large-eddy structures. Enhancement in heat transfer is seen in the stagnation region but this beneficial effect of vibration on heat transfer is confined to the impingement region, $r/D < 1.5$.

1 Introduction

Impinging jets have played a pivotal role in applications that require efficient heat- and mass-transfer. The canonical jet-impingement problem presents a deceptively simple configuration, yet produces a complex array of flow features. The analysis of impinging jets has grown in sophistication with improvements in experimental measurement techniques as well as numerical methods that enable powerful and accurate simulations by harnessing the rapid growth of affordable computing power.

Predicting accurate flow features of a jet impinging upon a stationary wall is in itself demanding considering the complex flow physics, which includes Kelvin-Helmholtz type shear layer development in the free-jet, a high static pressure region generated upon impingement, change in flow streamline curvature into the wall-jet region, development of a boundary layer along the wall and entrainment along the exit boundaries of the domain. Several studies have described these regions in detail along with their fluid flow and heat transfer characteristics. The reader is referred to the works of Martin [1], Jambunathan [2] and Viskanta [3] for exhaustive reviews on experimental jet-impingement studies. Conventionally, jet-impingement studies have either been performed with jets discharging cold fluid on a heated wall or conversely impingement of a hot fluid on a cold wall. Several studies have been performed on this fundamental configuration with changes to the geometry besides the fluid parameters. There have been few studies with impingement-wall vibrations (see [4], [5]), that focus predominantly on the heat transfer characteristics with inadequate or only qualitative data on the flow physics that cause heat-transfer variations on the impingement wall. Both augmentation and reduction in heat-transfer have been observed. Noticeably absent is information on the flow dynamics either at the near-wall region or elsewhere in the domain that is directly responsible for the

[1]Email address for correspondence: r.narayanaswamy@curtin.edu.au (Ramesh Narayanaswamy)

resulting thermal signatures on the impingement-wall in the context of forced convection. This has been overlooked by previous studies creating a gap in the understanding of the cause of the changes observed on the impingement-wall. The flow-physics spawned by a turbulent circular jet impinging upon a vibrating wall remains largely unknown. The present work attempts to close this gap by establishing the relationship between the flow features and the resulting heat-transfer on the impingement-wall.

A substantial amount of work has been carried out in analysing impinging jet configurations, in which the nozzle-to-wall distance (y/D), the jet Reynolds number, Re, inflow conditions of the jet, types of nozzles and number of jets issuing have been investigated in an extensive range of parametric combinations, with both experimental and numerical techniques. Cooper et al. [6] amongst many others were the first to present an in-depth experimental analysis of impinging jets with varying nozzle-to-wall spacings. Their experiments reported turbulent flow field statistics for varying nozzle-to-wall distances and Reynolds numbers. A companion paper to this work by Craft et al. [7] examined the development of eddy-viscosity models to model turbulence. Although the models initially demonstrated poor agreement in the stagnation region, improvements have been made to the turbulent viscosity parameters, yielding better agreement with experimental data [8]. Baughn and Shimizu [9] presented experimental results for a simple impinging jet flow, featuring an impingement wall that produced uniform heat flux. This work has proven valuable as benchmark for numerical work since uniform heat flux boundary conditions are straightforward to model. These results were later investigated numerically by several researchers including Yan and Saniei [10], Katti and Prabhu [11], Bovo and Davidson [12] for $Re = 23\,750$. The Nusselt number (Nu) is broadly used as an indicator of the heat-transfer rate on the impingement-wall. At small nozzle-to-wall distances, a secondary outer peak is observed in the radial distribution of the mean Nusselt number in addition to the primary inner peak within the stagnation region.

Analysis of the formation of a secondary Nu peak was conducted by Gardon and Akfirat [13] for various Reynolds numbers. They argued that a local thinning of the boundary layer was the cause of the secondary Nu peak. This was also observed in the work of Chung and Luo [14] for a laminar flow. They attributed the reduction in thermal boundary layer thickness to the large-scale interaction between the jet vortices and the impinging wall that resulted in the secondary Nu peak. Direct numerical simulations (DNS) of a laminar flow jet-impingement by Chung et al. [15] showed that heat-transfer at the impingement-wall is very unsteady and is mainly caused by the primary vortices emanating from the jet nozzle that interact with the wall shear layer. It was shown that the vortex location has a much stronger effect on Nu than the vortex strength. Although a correlation between the Nu and the flow field was seen, a breakdown in the Reynolds analogy was seen at downstream radial distances. Instantaneous skin friction coefficient, C_f and Nu variations show that local heat transfer distributions correlate closely with the flow fields. Recent DNS performed by Dairay et al. [16] for a turbulent jet with $Re = 10\,000$ showed that the primary and secondary vortices are responsible for the increased heat transfer since they constantly renew the wall with cold fluid due to their inherent induced velocity. This was also observed in the DNS of Rohlfs et al. [17] for a laminar flow Reynolds number.

In the recent experimental work of Tummers at al. [18], the turbulent characteristics of an impinging jet (Reynolds number comparable to [9]) were studied, and near-wall measurements revealed that flow reversals were related to the formation of secondary vortices. LES of these experiments were later conducted by Uddin et al. [19]. They used digital filtering of random data to generate the inflow velocity fluctuations. Hadžiabdić and Hanjalić [20] used inflow conditions from a pipe flow. However, only a quarter of the full three-dimensional domain was used in their LES study. They showed that the vortex roll-up phenomenon along the impingement-wall is the main event governing the flow. The connections between the convection of the primary vortices, the formation of the counter-rotating secondary vortices and the unsteady separation phenomena were elucidated. Also, a recent DNS study by Dairay et al.[16] states that the secondary Nusselt number peak becomes less pronounced when a long tube profile is used for the inflow. A similar observation has been made in the experimental work of Roux et al.[21] indicating a requirement for further investigation of this effect. A review of recent LES studies is available in Dewan et al. [22].

Tsubokura et al. [23] presented the development or transition of both plane and circular jets and identified the large-scale structures based on the Laplacian of pressure. They found that the eddy structures differed for the plane and circular jet configurations, and no organized structures were seen at the stagnation zone of the circular jet. Popiel and Trass [24] stated that the development of these large-scale vortex structures considerably enhanced the entrainment rate and mixing processes. An interaction of the well-ordered toroidal vortex structures convected downstream from a transient circular shear layer of a natural free-jet with the normally impinged flat wall was shown. It was inferred that these near-wall eddies are responsible for the additional enhancement of local momentum and heat or mass transfer. The wall eddies are rolled up on the wall between the large-scale toroidal vortices, which diverge in the radial direction.

It is evident from the aforementioned literature that events within the hydrodynamic boundary layer are largely accountable for the variations in the thermal characteristics of the impingement-wall. The boundary layer originates at the stagnation region and grows gradually, moving away from the stagnation region into the wall-jet region. Martin [1] reported that the thickness of the boundary layer δ_0, defined as the locus of the maxima of the wall-jet velocity in the stagnation zone would reach about one-hundredth of the nozzle diameter. The wall-jet profile formation occurs as a result of the simultaneous growth of wall boundary layer and the free-jet boundary. Since the boundary layer has a shearing influence upon the wall, increasing the shear on a stationary wall may be favourable in terms of increasing heat and mass transfer. This can be achieved by setting the impingement-wall in a periodic oscillatory motion perpendicular to the nozzle-exit, to modify the boundary layer formation and the corresponding events within it. A clear relationship between the vortical structures and their influence on the heated wall can be established since the vortical structures will oscillate (vertically) due to the wall motion.

Experimental work on vibrating impingement walls was first carried out by Ichimiya and Yoshida [4], for planar impinging jets. They considered the range of Reynolds numbers $1000 < Re < 10\,000$ and concluded that both enhancement and reduction of heat transfer could occur as a result of vibration. Numerically, Ichimiya and Watanabe [25] examined moderate Reynolds numbers of 200 and 500 and observed improved heat-transfer in the wall-jet region. Since the investigations were carried out for such low Reynolds numbers, the effect of turbulence, (which is a key contributor to heat transfer improvement) is neglected. Investigations by Hetsroni and Klein [26] used vibrations generated by a piezoelectric actuator for a micro liquid jet. An increase in heat-transfer was observed for micro-amplitudes. Wen [5] conducted experimental studies on impingement wall undergoing forced vibrations. The focus was on tubes with swirling strips and micro vibrations. The study concluded that the Nu was strongly dependent upon the wall vibration frequency, f, wall vibration amplitude, A, and the jet Reynolds number. However, a substantial dependence of the Nusselt number upon the nozzle-to-wall distance was not observed. Since smoke visualizations were used, the flow was analysed qualitatively. A detailed review of the literature shows that no concrete knowledge of the flow dynamics leading to changes in the Nu profiles has been established so far to the knowledge of the authors.

The present work attempts to provide insights into the flow dynamics and heat transfer when the impingement wall is subjected to forced excitation. A highly resolved computational fluid dynamics (CFD) dataset for this kernel flow-configuration is generated using LES. Also, fundamental understanding of the fluid dynamic behaviour arising from inherent and induced boundary-layer unsteadiness in jet-impingement is addressed. The changes to the thermal imprints on the heated wall are the major focus of the work. Wall-resolved LES of a circular jet impinging on a vibrating heated impingement-wall is presented along with other relevant validations for the methodology adopted. In the process, test cases are validated to assess the methodology that generates the data set. In the following, jet-impingement upon a static-wall is henceforth referred to as a static-wall jet-impingement configuration (abbreviated as SWJ) and the configuration where the impingement-wall undergoes forced vibration, or excitation, will be referred to as the vibrating-wall jet-impingement configuration (abbreviated as VWJ). The paper begins, §2, with a description of the governing equations employed, along with the solution control strategy, followed by a series of validations against established experiments starting with a pipe flow, a static-wall jet-impingement configuration in §3, and finally concluded with a vibrating-wall circular jet-impingement configuration. The flow dynamics and thermal characteristics of a vibrating-wall jet-impingement configuration is studied in §4, and concluding remarks are given in §5.

2 Numerical methods

2.1 Governing equations

The governing equations for the LES are the filtered continuity and incompressible Navier-Stokes equations given as,

$$\frac{\partial u_i}{\partial x_i} = 0, \tag{1}$$

$$\frac{\partial \overline{u}_i}{\partial t} + \frac{\partial (\overline{u}_i \overline{u}_j)}{\partial x_j} = -\frac{\partial \overline{p}}{\partial x_i} + \nu \frac{\partial}{\partial x_j}\left(\frac{\partial \overline{u}_i}{\partial x_j} + \frac{\partial \overline{u}_j}{\partial x_j}\right) - \frac{\partial \tau_{ij}}{\partial x_j} \tag{2}$$

for which the closure is provided with the dynamic Smagorinsky sub-grid scale (SGS) model [27, 28]. The SGS stress, τ_{ij}, is modelled since the resolved and unresolved scales interact through the SGS stress τ_{ij}. The dynamic Smagorinsky model approximates the SGS stress as,

$$\tau_{ij} - \tfrac{1}{3}\delta_{ij}\tau_{kk} = 2C_s\Delta^2|\overline{S}|\overline{S}_{ij} \tag{3}$$

where δ_{ij} is the Kronecker delta function. The sub-grid scale eddy-viscosity is given as $\nu_t = (C_s\Delta)^2|\overline{S}|$ where C_s is the Smagorinsky constant, Δ, the filter width governed by the mesh size ($\Delta = (\Delta V)^{\frac{1}{3}}$) and the magnitude of the strain rate tensor, $|\overline{S}| = (2(\overline{S_{ij}}\ \overline{S_{ij}}))^{1/2}$, $\overline{S_{ij}}$ is the rate of strain tensor of the resolved velocity field where $\overline{S}_{ij} = (\partial u_i/\partial x_j + \partial u_j/\partial x_i)/2$. The modified version of the dynamic Smagorinsky model takes into considerations the changes proposed by Lilly [28] for the dynamic computation of the Smagorinsky constant C_s.

2.2 Derived quantities for comparison

The convective heat transfer from the impingement wall is a function of the convective heat transfer coefficient h. Thus, a Nusselt number based on the heat transfer coefficient h and the diameter of the nozzle D is defined as

$$Nu = \frac{hD}{k} \tag{4}$$

where h is given as,

$$h = \frac{-k\partial T/\partial n}{T_{wall} - T_f} \tag{5}$$

where $\partial T/\partial n$ is the temperature gradient normal to the impingement wall, T_{wall} is the measured local wall temperature, T_f is the inlet temperature of the fluid and k is its corresponding thermal conductivity. The flow field is assumed to be unaffected by the temperature variations on the impingement wall and is advected by the fluid momentum along with molecular diffusion. Hence, the scalar transport equation for heat transfer can be solved with temperature as a passive scalar given by,

$$\frac{\partial T}{\partial t} + u_j\frac{\partial T}{\partial x_j} = \alpha\frac{\partial^2 T}{\partial {x_j}^2} \tag{6}$$

where α represents the thermal diffusivity and is given as $(\nu/Pr + \nu_t/Pr_t)$. Pr and Pr_t are the laminar and turbulent Prandtl numbers, given respectively by $Pr = 0.74$ and $Pr_t = 0.85$, and ν and ν_t are their corresponding viscosities.

2.3 Solution control

The simulations were performed using LES with the C++ code Open Field Operation and Manipulation (OpenFOAM) to solve the incompressible Navier–Stokes equations. Equations 1 and 2 are discretised on a non-uniform collocated Cartesian grid. A second-order accurate backward implicit scheme for time discretisation is used. The convection terms are discretised by a second-order accurate central differencing scheme. The pressure-velocity coupling is solved with PISO–SIMPLE (PIMPLE), an algorithm that merges Pressure Implicit with Splitting of Operator algorithm (PISO) and a Semi-Implicit Method for Pressure-Linked Equations (SIMPLE) algorithm that allows the calculation of pressure on a mesh from velocity components by coupling the Navier–Stokes equations through iterations. The PIMPLE algorithm is composed of an implicit momentum predictor and several pressure–velocity correctors. The velocity and pressure are corrected in loops to ensure that the continuity equation is satisfied. This method also ensures an oscillation-free velocity field with an implicit treatment in line with the Rhie–Chow correction [29]. The temporal resolution is dynamically adjusted through a variable time-stepping technique such that the Courant-Friedrich-Lewy (CFL) number was less than or equal to 0.5 at all times. The code is parallelized using the Message Passing Interface (MPI) protocol and the graph partitioning algorithm SCOTCH [30] was used to decompose the solution domain into the required number of sub-domains for parallel computing. The algorithm has been widely tested and accounts for the differing performances among processors. Since this algorithm reduces the number of processor boundaries, thus reducing the interconnect message passing, it results in higher performance. The simulations were carried out on MAGNUS, a Cray XC40 supercomputing system located at the Pawsey Supercomputing Centre, Western Australia.

3 System development and validation

The vibrating-wall jet-impingement system is assembled through the combination of a set of sub-systems. First, to establish the method of generating fully developed turbulent inflow boundary conditions, a turbulent pipe flow simulation is validated against the experiments of Toonder et al. [31]. Second, to establish the static-wall impinging jet configuration (SWJ), validation against the experiments of Cooper et al. [6] and other established works is performed. Finally, these elements are combined to create the computational model of the vibrating-wall jet-impingement configuration (VWJ).

3.1 Inflow

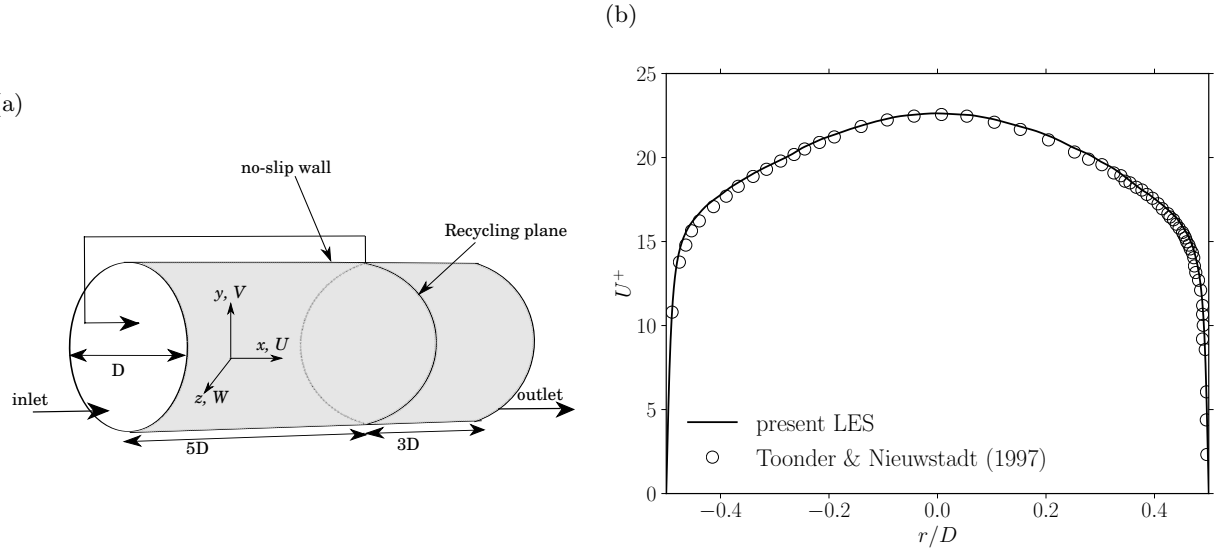

Figure 1: (a) Schematic representation of the turbulent pipe flow geometry and the coordinate system used for the simulations, and (b) mean velocity U^+ as a function of r/D for a turbulent pipe flow. ——: present LES at $Re_D = 24\,600$; ○: Toonder & Nieuwstadt [31] at $Re_D = 24\,600$.

In experiments, fully developed flows are commonly generated by having sufficiently long pipe lengths. To replicate this physical phenomenon in a computational model, it is customary to use data from the exit plane of a pipe flow simulation or a precomputed library technique to account for the velocity scales at the nozzle-exit at each time-step. It is necessary that the flow be invariant in the flow direction. However, this method requires two separate simulations and a re-run of any precursor pipe flow simulations for small changes when varying the inlet parameters of the jet-impingement simulation.

In the present modelling, the inflow conditions are generated by a similar method except that it is performed simultaneously in a single simulation. Precursor calculations are performed at a recycle plane downstream of the pipe flow inlet, and transient data from this sample plane is fed back to the inlet at every time-step [32]. This method creates a fully developed turbulent velocity profile at the outflow of the pipe due to the flow loop, resembling an infinitely long pipe. However, this technique can be open to non-physical interactions between the recycle plane and the inlet and may introduce periodicity and streamwise repetition of flow features [33]. To evaluate this technique, LES of an incompressible fully developed turbulent pipe flow is carried out comparable to the experiments of Toonder and Nieuwstadt [31]. The Reynolds number based on the pipe diameter defined as $Re_D = U_b D/\nu$ was set to 24 600 and the corresponding Kármán number based on friction velocity is defined as $R^+ = u_\tau R/\nu$ is 690, where $u_\tau = (\tau_w/\rho)^{1/2}$, R is the pipe radius, τ_w is the wall shear stress and ρ the density.

A schematic representation of the pipe flow geometry and the coordinate system used is shown in figure 1(a). The computation was performed on a finite volume mesh of 600 × 240 × 240 grid points along the x, y and z directions respectively where x is the axial flow direction, y the radial coordinate, and z the azimuthal coordinate. The mean velocity components (U, V, W) and the fluctuating components (u, v, w) are solved based on the solution control described in §2.3. The superscript + represents quantities scaled by friction velocity u_τ for velocity components and the viscous length scale $\delta_{nu} = \nu/u_\tau$ for the distance. Previous experiments have reported the maximum wavelength of large-scale motions ranging from $4D$ to

$8D$ (see [34], [35]) and several DNS studies utilized this range of domain length for their simulations (see [36], [37]). Accordingly, the domain length, L, of the pipe is $8D$ and the recycle plane was located at $5D$ from the inlet. The mesh was refined close to the walls so that the non-dimensional wall distance, $(1-r)^+ < 1$. No-slip boundary conditions were used on the walls, and a pressure outlet boundary was prescribed at the outlet. The results are time-averaged along the entire length of the domain and converted to a $2D$ plane by an azimuthal average.

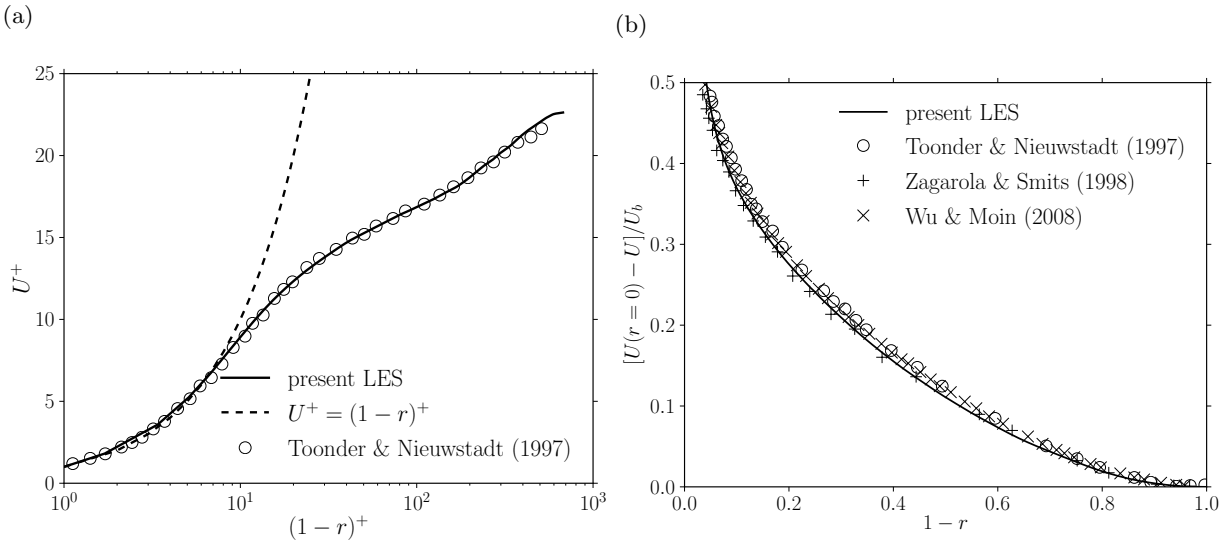

Figure 2: (a) Mean velocity U^+ as a function of $(1-r)^+$. ——: present LES at $Re_D = 24\,600$; - - - -: $U^+ = (1-r)^+$; ○: Toonder & Nieuwstadt [31] at $Re_D = 24\,600$, and (b) mean velocity defect, $[U(r=0)-U]/U_b$ as a function of $(1-r)$. ——: present LES at $Re_D = 24\,600$; ○: Toonder & Nieuwstadt [31] at $Re_D = 24\,600$; +: Zagarola & Smits [38] at $Re_D = 31\,000$; ×: Wu & Moin [36] at $Re_D = 44\,000$.

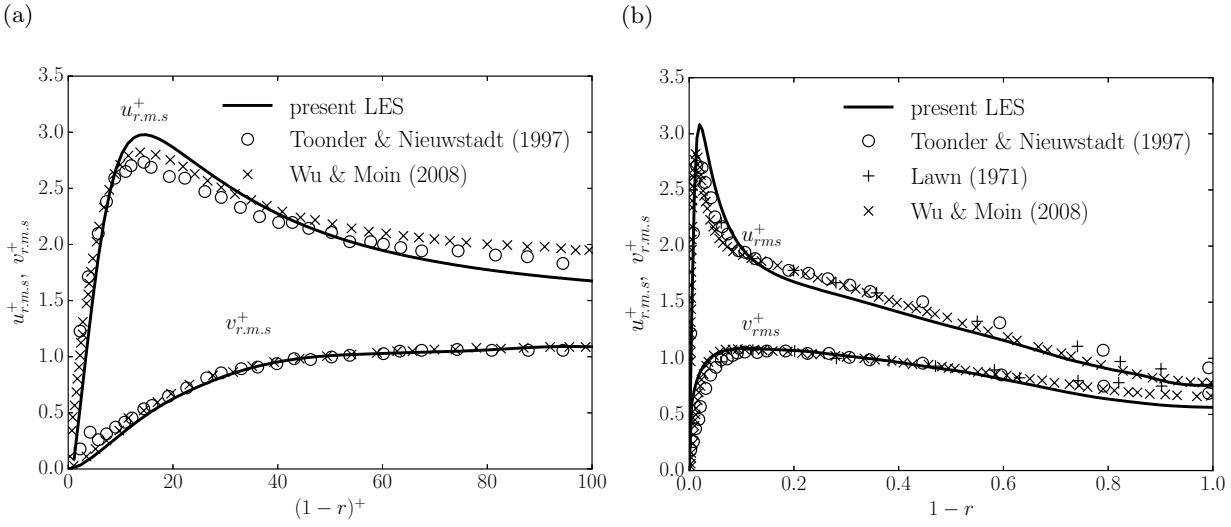

Figure 3: (a) Axial and radial r.m.s velocity profiles as a function of $(1-r)^+$ in the near-wall region.——: present LES at $Re_D = 24\,600$; ○: Toonder & Nieuwstadt [31] at $Re_D = 24\,600$; ×: Wu & Moin [36] at $Re_D = 44\,000$, and (b) axial and radial r.m.s velocity profiles as a function of radial coordinate $(1-r)$. ——: present LES at $Re_D = 24\,600$; ○: Toonder & Nieuwstadt [31] at $Re_D = 24\,600$; +: Lawn [39] at $Re_D = 38\,000$; ×: Wu & Moin [36] at $Re_D = 44\,000$.

Figure 1(b) shows the mean axial velocity profile over the cross section of the pipe compared against the experiments of Toonder and Nieuwstadt [31]. A fully developed symmetric mean flow velocity profile is achieved and is in good agreement with the experimental data. Mean velocity statistics at the near-wall region as a function of wall units $(1-r)^+$ is shown in figure 2(a). The resolution chosen for the simulation proves to be adequate as seen in the log-law profile for the mean axial velocity. The profile follows the law of the wall and accurately predicts the velocity within the viscous sub-layer ($(1-r)^+ < 5$). Further into the buffer layer and the outer layer, excellent agreement is observed with the experimental data. To enable

comparison across a range of Re_D and partially due to the invalidity of the universal velocity defect law, Wu & Moin [36] used the mean velocity defect, $[U(r=0)-U]/U_b$, normalized by the bulk velocity, U_b. The trend of the mean velocity defect for the outer layer is shown in figure 2(b). The velocity defect is high closer to the wall and gradually vanishes on moving towards the pipe axis. The results show excellent agreement with the experimental data of Toonder and Nieuwstadt [31](Re_D = 24600), Zagarola & Smits [38](Re_D = 31 000), and the DNS of Wu & Moin [36](Re_D = 44 000).

The root-mean-square (r.m.s) values of the fluctuating components of velocity normalized by u_τ, as a function of inner wall units $(1-r)^+$ are shown in figure 3(a). Good agreement is observed between the experimental data of Toonder and Nieuwstadt [31](Re_D = 24 600), the DNS of Wu & Moin [36](Re_D = 44 000) and the current LES. The computed values of the axial and radial fluctuations are predicted accurately using the present numerical framework. The peak values and the location of the fluctuations agree well with the previously mentioned studies (see [36], [37]). In figure 3(b), the turbulence intensities are shown across the outer unit $(1-r)$, and compared with the experimental data sets of Nieuwstadt [31](Re_D = 24 600) and Lawn [39](Re_D = 38 000) along with the DNS of Wu & Moin [36](Re_D = 44 000) for completeness. The axial fluctuation is marginally under predicted in the radial range of $0.2 < (1-r) < 0.4$ however, the radial fluctuation has very good agreement with the representative data across the entire range.

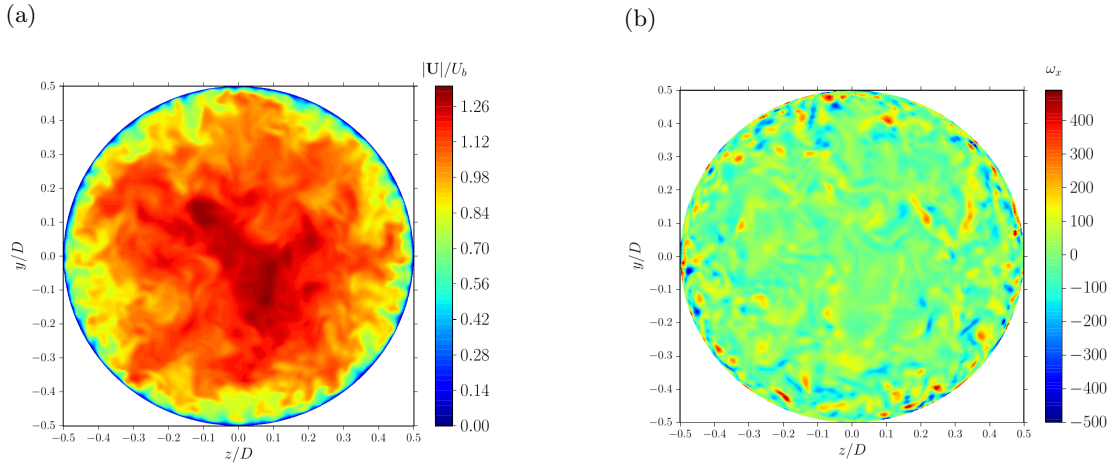

Figure 4: Visualization of the turbulent pipe flow at Re_D = 24 600 over a constant x plane with contours of (a) instantaneous velocity magnitude, $|\mathbf{U}|$ normalized by bulk velocity, U_b, and (b) instantaneous streamwise vorticity (ω_x).

To demonstrate that the flow structures are preserved, the instantaneous velocity and vorticity profiles in a cross-sectional plane of the pipe are visualized in figures 4(a) and (b) in which the contours of instantaneous velocity magnitude, $|\mathbf{U}|$ normalized by the bulk velocity, U_b along with the vorticity in the streamwise direction (ω_x) are presented for the same location of the plane at the same instant in time. The characteristic mushroom-shaped bulges with lower fluid velocity appear closer to the wall and on moving closer to the pipe core, the structures of the fluid are more disordered and exhibit high momentum as expected. The vorticity profile shows more counter-rotating vortices closer to the pipe wall than at the pipe core as expected.

Overall, the mean and instantaneous turbulent characteristics are in good agreement with the experimental data and the flow structures are well preserved. These results indicate that the computed LES of an incompressible turbulent flow in a smooth pipe at Re_D = 24 600 with a recycled inflow boundary condition can be adopted to generate a fully developed turbulent inflow for simulations needing such inlet conditions without having to run redundant pipe flow simulations externally.

3.2 Static-wall circular jet-impingement configuration (SWJ)

The preceding turbulent inflow generation method is now used for the validation of an incompressible turbulent unconfined circular jet-impingement on a stationary wall with uniform heat flux. Large-eddy simulations are performed for a jet Reynolds number of Re = 23 000 with a nozzle-to-wall distance of $2D$. The variables are chosen in order to replicate configurations from previous studies. Several experimental and numerical studies exist for the configuration mentioned above. The experimental measurements of Cooper

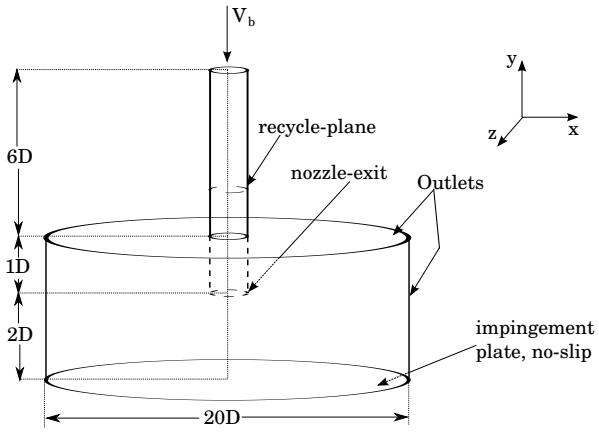

Figure 5: Schematic representation of the circular jet impingement configuration with the boundary conditions and the coordinate system used for the simulations.

Grids	Pipe ($2D < L_y < 9D$, $0 < r < 0.5D$)				Impingement Domain ($0 < L_y < 2D$, $0 < r < 10D$)				Top Free Boundary ($2D < L_y < 3D$, $0.5D < r < 10D$)			
	N_r	N_y	N_θ	Total	N_r	N_y	N_θ	Total	N_r	N_y	N_θ	Total
Grid-I	112	200	180	4×10^6	309	136	180	7.5×10^6	195	57	180	2×10^6
Grid-II	147	200	260	7.6×10^6	391	136	260	14×10^6	240	25	260	1.5×10^6
Grid-III	190	180	640	22×10^6	354	150	640	34×10^6	260	25	640	4.1×10^6

Table 1: Grid parameters for the computational domain.

et al.[6] are used as a reference. The experiments of Tummers et al. [18], Geers et al. [40], Baughn and Shimizu [9] and, Yan and Saniei [10] are also presented alongside the current LES results for comparison.

A schematic of the flow configuration is presented in figure 5. The solution domain is a collocated grid system with Cartesian coordinates, $\mathbf{X} = (x, y, z)$; with 0 as the origin at the center of the domain Ω, where $\Omega = [0, r] \times [0, L_y]$ with $L_y = 9D$ and the radius, $r = 10D$. The instantaneous velocity components are denoted $\mathbf{u} = (u, v, w)$ and the mean velocity components are denoted by $\mathbf{U} = (U, V, W)$. In the (x, y)-plane, the radial direction $r = \sqrt{x^2 + z^2}$ is given by x (at azimuthal direction, $z = 0$) and the azimuthal angle $\theta = \arctan(x/z)$. The Reynolds number based on the jet-nozzle diameter D, bulk velocity V_b, and the kinematic viscosity ν is given as $Re = V_b\ D/\nu = 23\,000$. The accuracy of LES tends to a DNS with increasing spatial resolution and reducing filter width. We, therefore, investigate the acceptable levels of mesh resolution for the current configuration.

At the inlet, fully-developed turbulent flow is generated by the recycle plane at an upstream distance of $1D$ from the nozzle-exit. At the impingement wall, $y = 0$, a Dirichlet (no-slip) boundary condition is applied hence $\mathbf{U}(x, y = 0, z, t) = 0$. For pressure, a Neumann boundary condition is used which implies $\partial p/\partial y = (x, y = 0, z) = 0$ and a uniform heat-flux boundary condition is applied at the wall for temperature. On the bounding sides of the domain (i.e., $r/D = \pm 10$, and $y/D = L_y/3$), a mixed boundary condition is applied for velocity where $\mathbf{U}$ is evaluated from the flux when the pressure is known. With this boundary condition, for an inbound flow, the velocity is obtained using the flux from the first adjacent cell of the boundary and for outward flow, a zero-gradient is applied. A Dirichlet boundary condition is applied for pressure at the outlets, using the reference pressure of the flow field, $p_0 = p + 0.5|U|^2$, where p_0 is the stagnation pressure, and p is the static pressure at the boundary and is dependent upon $\mathbf{U}$. Turbulence statistics are averaged in space and time after ten flow cycles where one flow cycle means that a fluid particle has travelled through the axial and radial dimensions i.e. $9D + 10D$ at the bulk velocity, V_b. The statistical averaging continues for 30 flow cycles. The entire domain was initialized with a converged Reynolds-averaged Navier–Stokes (RANS) simulation.

Three grids are considered for the sensitivity analysis for which the grid parameters are given in Table 1. All three grids were discretised with hexahedral control volumes and were generated with the native

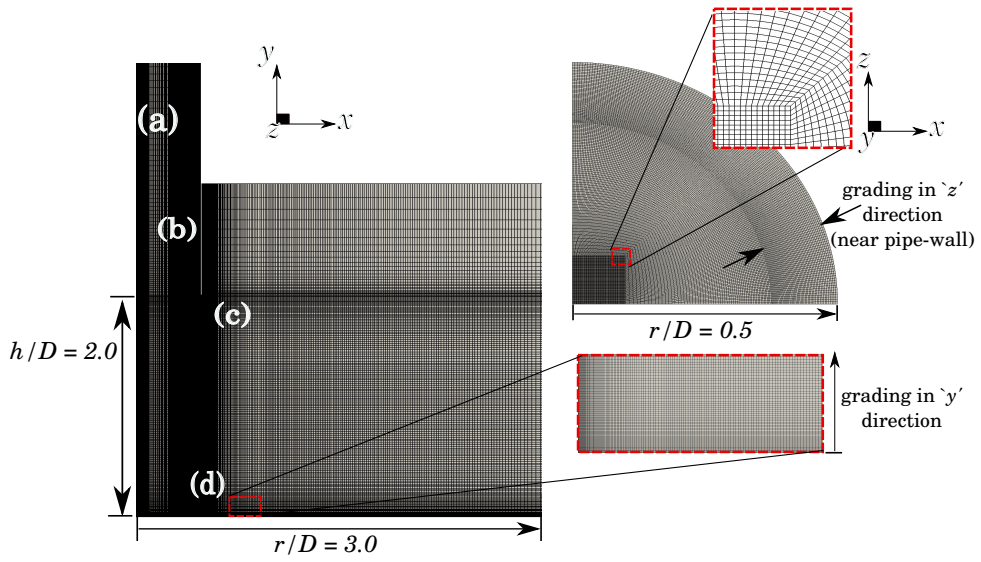

Figure 6: Plane and top view of the mesh segments showing critical zones (a)-(d), where zone (a) represents the pipe centreline, (b) the pipe near-wall, (c) the periphery of the nozzle-exit, and (d) the near-wall of the domain respectively.

OpenFOAM mesh utility, 'blockMesh'. The 'blockMesh' utility uses a separate dictionary to divide the domain into one or more hexahedral blocks and the vertices and edges can be modified based on the requirement. The present computational domain is chiefly divided into three blocks, namely the pipe, the impingement domain, and the top boundary. Since the number of cells varies among these blocks, they are listed individually and allow for a realistic comparison with other jet-impingement computational set-ups which tend to use inflow without a fully developed pipe, or the top open boundary replaced with confinement. Grid-I was the coarsest mesh used with a total of 13.5×10^6 cells. The grid had 180 cells in the azimuthal direction. However, this was not sufficient to predict the mean-flow characteristics accurately. Grid-II was generated with approximately twice the number of cells of Grid-I, clustering cells in both the radial and azimuthal directions. Although the fluid-flow results improved substantially, the Nusselt number data were under-predicted indicating the need for increased resolution in the azimuthal direction. Grid-III was generated with three times the number of cells in the azimuthal direction as compared to Grid-II with 60×10^6 cells. The results obtained with these grids are discussed in §3.3.1 to §3.3.3

A plane view of the grid (Grid-III) is shown in figure 6 with crucial zones identified within the domain as (a) to (d). Zone (a) in the domain refers to the pipe centreline ($0 < r < 0.3D, 0 < L_y < 9D$) where care was taken to cluster the cells from the inlet to the stagnation zone. The circular shape of the domain was discretised with a 'butterfly' mesh topology that is based on a square outline at the centre and is gradually modified into the circular shape. A geometric expansion ratio of the mesh was maintained below 1.2 for the mesh to expand smoothly in the radial direction in the critical areas of interest. Zone (b) is the region close to the pipe/nozzle wall region ($0.3 < r < 0.5D, 0 < L_y < 9D$) where the mesh was finely graded from the nozzle wall towards the axis centreline. It is critical to have a fine mesh in this area to resolve the near-wall statistics of the inflow such as axial-and the wall-normal components of fluctuations which directly influence the impingement-wall heat-transfer. Zone (c) is the region ($1.75D < L_y < 2.2D$) immediately at the nozzle exit, arrayed with cells and graded with a finer mesh so that the instabilities generated due to the shear and sudden expansion of the fluid upon exit are captured effectively. These small-scale phenomena on traversing axially downward, grow and expand radially upon impingement causing crucial changes to the wall heat-transfer. Finally, in Zone (d), which is the near-wall region, the cells are configured in uniform annular layers and graded such that maximum $y^+_{wall} \approx 1.0$ which is within the viscous sub-layer. The majority of the cells were arrayed within the region $0 < L_y < 1D$ and $-4D < r < 4D$ so as to resolve the shear layer development. All the grids are discretised with hexahedral control volumes.

Pope [41] suggested that 80% of the energy must be resolved everywhere for LES with near-wall resolution. To assess the resolved kinetic energy in the domain, the current LESs are analysed based on the quality index proposed by Celik et al.[42] for which the filter length is implicitly related to the grid cell size and with second-order accuracy in time and space and can be independent of experimental or DNS data. The test for the quality index is based on the use of turbulent kinetic energy resolved (k_{res}) versus the

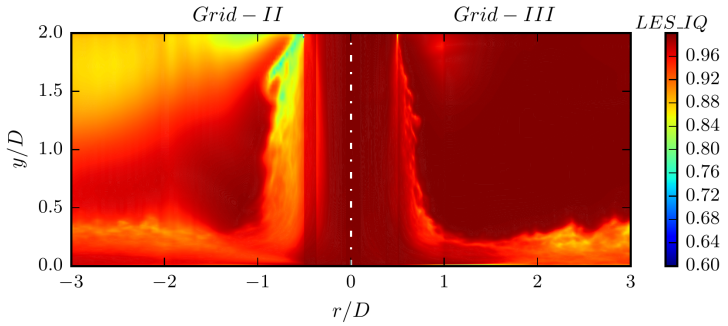

Figure 7: Map of resolvedness in the computational domain for Grid-II and Grid-III.

total turbulent kinetic energy (k_{tot}). Thus, the quality index or the resolvedness can be defined as,

$$LES\_IQ = \frac{k^{res}}{k^{tot}} = \frac{k^{res}}{k^{res} + k^{SGS}} \tag{7}$$

where $k_{res} = \frac{1}{2}(\overline{u'^2} + \overline{v'^2} + \overline{w'^2})$. The contour plot of the LES quality index or the resolvedness for Grids-II and III are shown in figure 7. It can be seen that in general, the critical zones of the domain are well resolved and greater than 90% for Grid-III. However, for Grid-II, some regions are marginally under-resolved. The first region of interest is the region around the nozzle exit (Zone (c)). It can be seen that in the immediate vicinity of the nozzle exit, there is a region of under resolvedness. The quality index in this region drops to well below 75%. This is due to the fact that there is a sudden expansion in the flow which induces substantial dissipation near the nozzle exit region; Grid-II is not refined enough at the nozzle-exit to represent this phenomenon. Grid-III does not show any such anomalies within the domain and the grid is sufficiently resolved since this region is complemented by a local refinement in the mesh. The region experiences a sharp gradient in the flow. Because of the development of the radial wall jet and the Kelvin-Helmholtz instabilities formed due to the shear layer, the prediction of the turbulent kinetic energy though within acceptable range, requires a mesh close to the Kolmogorov microscales to resolve the finest scales. However, the simulation, in general, has a high quality index throughout the domain indicating good resolution in the quality of the results.

3.3 Results (Static-wall circular jet-impingement configuration)

3.3.1 Instantaneous and mean flow statistics

Figure 8(a) shows the base flow of the jet via contours of the instantaneous velocity magnitude normalized by bulk velocity, V_b for $Re_D = 23\,000$. The flow exits the nozzle from the top of the figure and develops as a free-jet creating a shear layer with the quiescent fluid. The flow travels downstream (towards the static-wall) forming a free-jet and is seen to impinge on the wall creating a high pressure stagnation region. Upon impingement, the free-jet deflects and spreads radially as a wall-jet increasing the boundary layer thickness. Deceleration of the velocity field is seen on moving downstream from the stagnation region. Figure 8(b) shows the magnitude of instantaneous pressure field in the domain. Low-pressure regions within the shear-layer indicating the eddy roll-up are seen to travel axially downward and deflect radially upon impingement. A local high-pressure region is seen at the stagnation region due to impingement. The interplay with the stationary fluid is visualized through the instantaneous magnitude of vorticity, $(\omega_i\omega_i)^{0.5}$ in figure 8(c) where the jet upon exit starts to develop vortices of Kelvin-Helmholtz type due to interactions with the stagnant fluid shown as horizontal planes at varying locations in the free-jet. In the vicinity of the jet exit ($y/D = 1.95$), the vortex ring is slim and does not show any distinct vortical features. However, on travelling axially downward, the vortex ring develops instabilities upon interaction with the quiescent fluid. The 'vortical nests' as referred to by Hadžiabdić and Hanjalić [20] are seen to increase with the increase in axial distance from the jet-exit. It is essential that the ring vortex is captured effectively because these vortical structures travelling axially downward, tend to grow by stretching and eventually break down before impinging on the surface at different time instants creating multiple local hot-spots of increased heat transfer. All the contours presented above are for the same instant in time for Grid-III.

The isosurfaces of the Q-criterion are shown in figure 9 in which the Q-criterion is coloured by the distance from the impingement wall. The isosurfaces suggest that the slender small-scale structures are

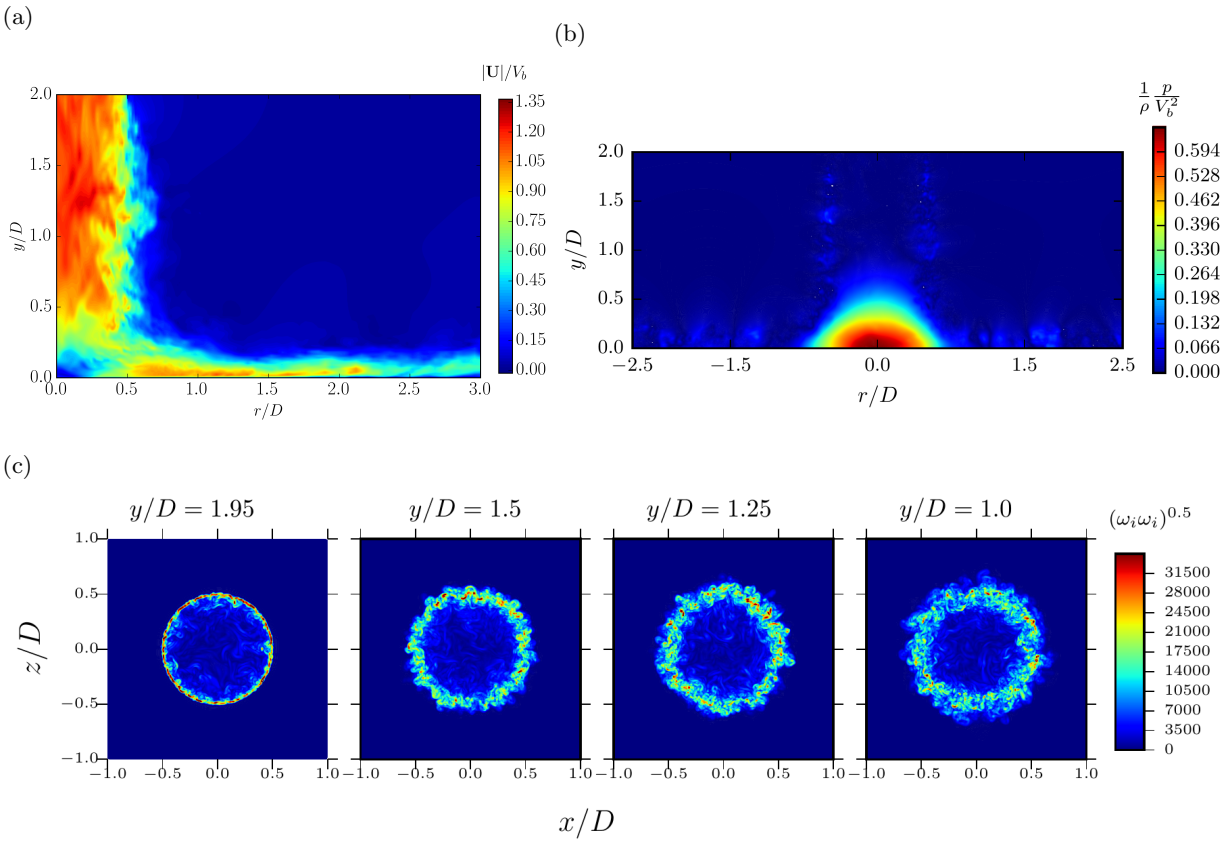

Figure 8: Visualization of circular jet impingement at Re_D =23 000 over a constant z plane with contours of (a) instantaneous velocity magnitude, $|\mathbf{U}|$, normalized by bulk velocity, V_b, (b) instantaneous pressure field, and (c) Instantaneous total vorticity magnitude, $(\omega_i\omega_i)^{0.5}$ in four horizontal planes ($y/D = 1.95, 1.5, 1.25$ and 1.0) in the free jet zone.(Note: 'y' is measured from the impingement plane.)

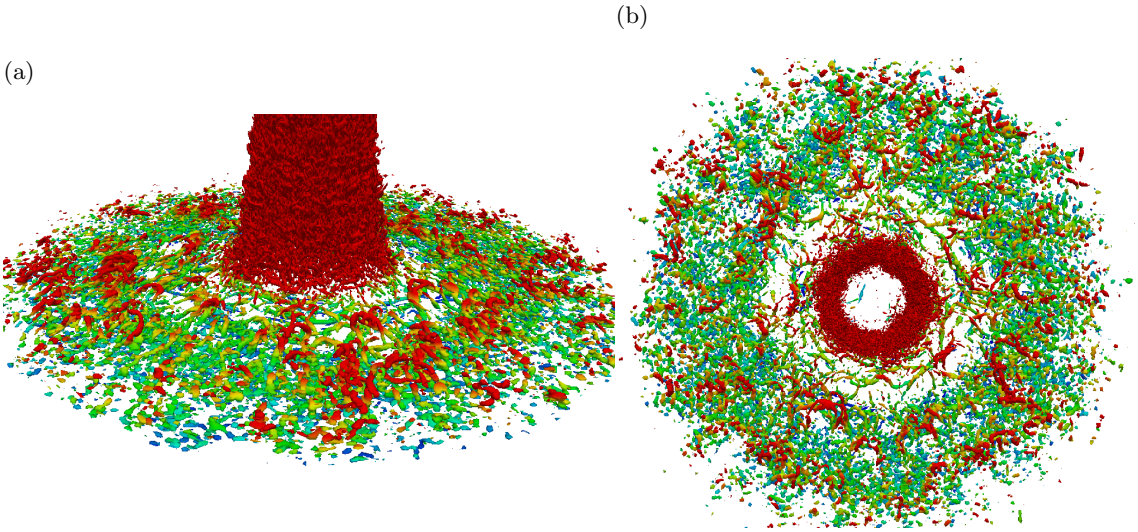

Figure 9: Isosurfaces of the Q-criterion ($Q = 30V_b^2/D^2$) for the subdomain $4D \times 2D \times 4D$ with the colours corresponding to the distance y/D from the impingement wall (blue - $y/D = 0$ and red - $y/D = 0.3$), (a) Perspective view, and in (b) Top view

captured efficiently and are oriented along the radial direction. It shows the presence of large-scale structures close to the stagnation region. The small-scale arrangement is also seen in the immediate vicinity of the jets which tend to form the braid regions along the shear layer of the jet. The toroidal organisation of the flow is also visible.

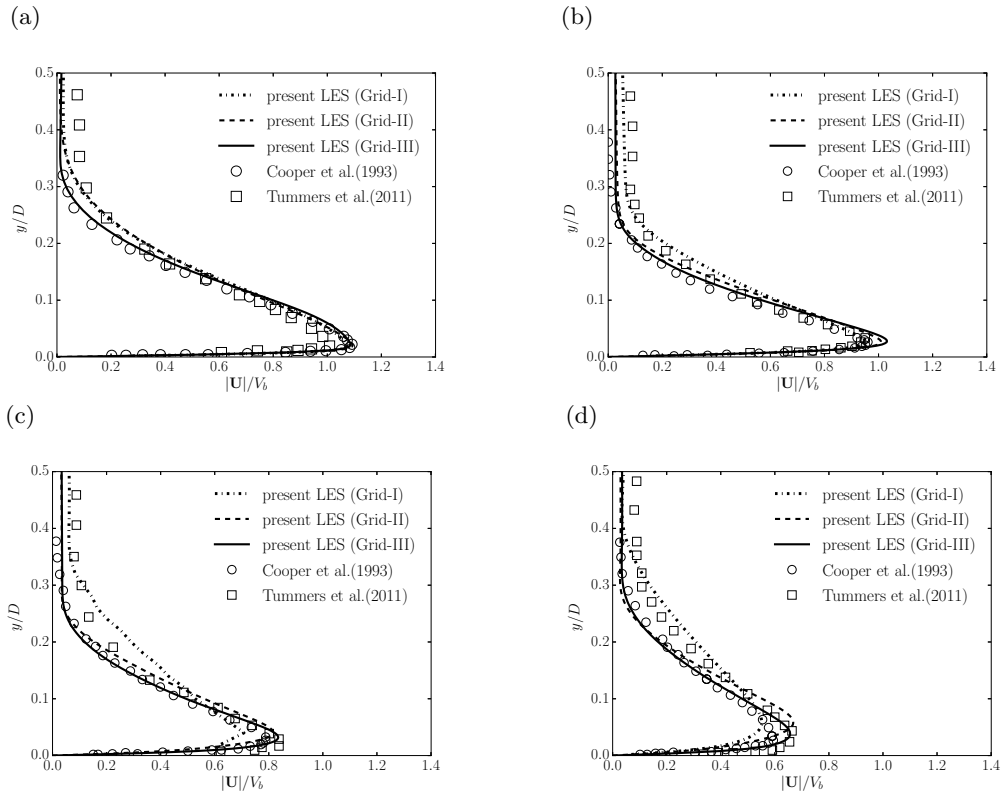

Figure 10: Development of mean velocity profile in the near-wall region at (a) $r/D = 1.0$ (b) $r/D = 1.5$ (c) $r/D = 2.0$ (d) $r/D = 2.5$. ——: present LES at $Re_D = 23\,000$ using Grid-III; - - - - -: present LES at $Re_D = 23\,000$ using Grid-II;— · — · —: present LES at $Re_D = 23\,000$ using Grid-I; ○: Cooper at al. [6] at $Re_D = 23\,000$; □: Tummers et al. [18] at $Re_D = 23\,000$.

The development of the mean velocity magnitude profile normal to the wall for the results of figure 8 is shown in figure 10. The mean velocity is normalized by the bulk velocity, V_b, and the vertical distance, y, is normalized by the jet nozzle diameter, D. The results presented for the SWJ are averaged in time and the azimuthal direction. The data is compared with the experiments of Cooper et al. [6] and Tummers et al. [18]. The experiments of Cooper et al. [6] were carried out with hot-wire anemometry with an experimental uncertainty of $\pm 2\,\%$ for the bulk velocity V_b. The results of the present simulation are in good agreement with these experimental works. The spatial development of the wall-jet is seen as the mean flow reaches a maximum between $r/D = 1$ to 1.5 and then begins to decelerate on developing into the wall-jet region losing its momentum on radial spreading. The results of Grid-II at $r/D = 1$ are almost identical to those of Grid-III. However, on moving radially downstream from the stagnation region ($r/D > 1$), the importance of radial resolution is evident through a poor agreement with Grid-I compared with the reference data set. Grid-III gives better agreement with the experiments compared to Grid-I and II particularly in the near-wall ($y/D < 0.1$) region due to the higher spatial resolution of the mesh. For $y/D > 0.8$, the mean velocity remains largely unaffected since the shear layer has a weak influence on the centre of the jet.

3.3.2 Second-order turbulence statistics

The distribution of the radial r.m.s velocity normalized by the bulk velocity, V_b is shown in figure 11(a). The LES predictions are compared to the experimental work of Cooper et al. [6] along with the LES of Hallqvist [43] ($Re_D = 20\,000$) within the shear layer. The present levels of u_{rms} are in good agreement. Peak values of u_{rms} are seen at the radial distance $r/D = 1.5$ to 2.2. This location of the u_{rms} peak is identical to the peak-value location of the turbulent kinetic energy shown in figure 11(b). The near-wall fluctuations of the simulation are in agreement with experimental measurements. The values of u_{rms} increase from $r/D = 0.5$ owing to the acceleration of the flow in the wall-jet region. In the vicinity of the

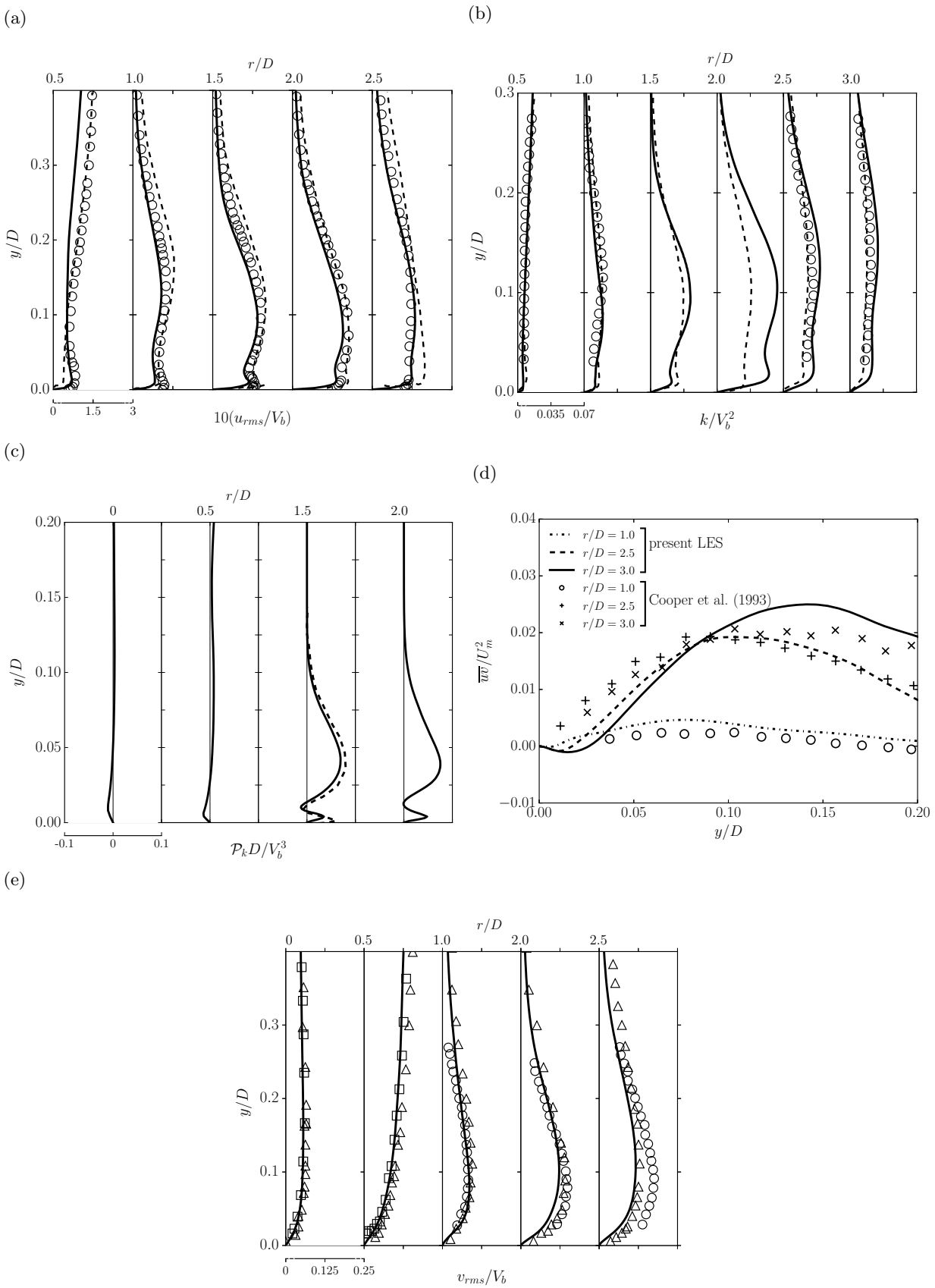

Figure 11: (a) Development of root mean square radial velocities in the near-wall region. ——: present LES at Re_D = 23 000 using Grid-III; - - - -: Halqvist [43] at Re_D = 20 000; ○: Cooper et al. [6] at Re_D = 23 000 (b) development of turbulent kinetic energy profiles in the near-wall region. ——: present LES at Re_D = 23 000 using Grid-III; - - - -: Hadžiabdić and Hanjalić [20] at Re_D = 20 000; ○: Cooper et al. [6] at Re_D = 23 000, (c) production of turbulence kinetic energy at different radial locations for the SWJ compared with the LES of Hadžiabdić and Hanjalić (dashed lines) at r/D = 1.5, and (d) turbulent shear stress $\overline{uv}$ at different radial locations. lines: present LES at Re_D = 23 000 using Grid-III; symbols: Cooper et al. [6] at Re_D = 23 000, and (e) wall-normal root mean square velocity profiles. ——: present LES at Re_D = 23 000 using Grid-III; ○: Cooper et al. [6]; △: Tummers et al. [18] at Re_D = 23 000; □: Geers et al. [40] at Re_D = 23 000.

wall, the viscous dissipation reduces the levels of u_{rms} and as the radial distance increases, the fluctuations decrease further due to the wall blocking effect.

The evolution of turbulent kinetic energy normalized by the square of the bulk velocity, V_b along the radial direction is shown in figure 11(b). The results are compared with the experimental work of Cooper et al. [6] and the numerical work of Hadžiabdić and Hanjalić [20] ($Re_D = 20\,000$) within the shear layer. Good agreement is observed with both these experimental and numerical studies. The acceleration region where the turbulent kinetic energy attains a peak value in the wall-jet region is from $r/D = 1.5$ through to $r/D = 2.2$. This increase of the turbulent kinetic energy in the wall-jet region is due to the high shear and rapid acceleration of the flow due to strong streamline curvature. This peak in the turbulent kinetic energy matches the numerical findings of Uddin et al. [19] and experimental findings of Lytle and Webb [44] who linked this increased turbulent kinetic energy to the formation of the secondary Nu peak. Double peaks are observed in the region $1.5 < r/D < 2.0$, but the peak values are marginally higher compared to those obtained by Hadžiabdić and Hanjalić [20]. To complement the analysis of the turbulent kinetic energy, the budgets of turbulent kinetic energy have been analysed. Figure 11(c) shows the turbulence production ($\mathcal{P}_k = -\overline{u_i' u_j'}\partial u_i/\partial x_j$) along the radial direction for the static wall configuration. In the stagnation region, negative production of turbulence kinetic energy was observed by previous experiments [see [45], [40]] and numerical studies [see [46], [20]] indicating the energy transfer back to the mean field from the turbulent field. This has also been confirmed in the present investigation (see figure R 5) for the static-wall case. For comparison, the LES data of Hadžiabdić and Hanjalić is plotted at $r/D = 1.5$ where the maximum turbulence kinetic energy is observed. Good agreement is observed and the characteristic twin peaks are reproduced.

Figure 11(d) shows the turbulent shear stress profiles of the SWJ normalized by the square of the maximum radial velocity, U_m in the wall-jet. The LES predictions are compared to the measurements of Cooper et al. [6]. The results compare well with the prediction of the level of shear stresses. The negative maximum shear stress values obtained are consistent with the values obtained by Hadžiabdić and Hanjalić [20]. With increasing radial distance, the value of the negative shear stress tends to increase. Hadžiabdić and Hanjalić observed that the maximum wall-jet velocity was not proportional to the minimum shear stress value. This is also seen in the present work, for example, at $r/D = 2.5$ the shear stress value is higher compared to $r/D = 1.0$ but the wall-jet velocity gradient is lower compared to that at $r/D = 1.0$. Due to the turbulent pipe flow boundary condition at the inlet, the wall jet region remains turbulent in all radial positions, and no relaminarisation or transition to turbulence occurs.

The profiles of wall-normal velocity fluctuations of the SWJ normalized by the bulk velocity are shown in Figure 11(e). The present LES results are compared with the experiments of Cooper et al. [6], Tummers et al. [18] and Geers et al. [40]. The good correspondence with the experiments is reflected by the accurate predictions of the impingement-wall heat-transfer discussed in the following section.

3.3.3 Heat-transfer characteristics

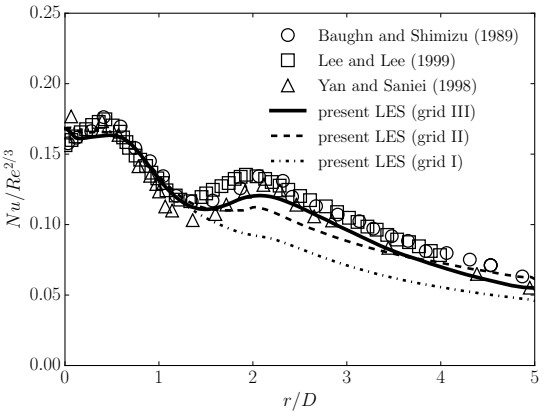

Figure 12: Time-averaged and normalized Nusselt number, $Nu/Re^{2/3}$ on the impingement wall as a function of radial distance r/D. ——: present LES at $Re_D = 23\,000$ using Grid-III; - - - - -: present LES at $Re_D = 23\,000$ using Grid-II;– · – · –: present LES at $Re_D = 23\,000$ using Grid-I; ○: Baughn & Shimizu [9] at $Re_D = 23\,750$; □: Lee & Lee [47] at $Re_D = 20\,000$; △: Yan and Saniei. [10] at $Re_D = 23\,340$.

The time and azimuthal averaged Nu predicted from the current LES is presented here. Normalization of Nu by $Re^{2/3}$ was proposed by Martin [1] to remove the influence of Reynolds number. This normalization has been used in the current work to enable direct comparison of diverse data sets. Works that have previously adopted this normalization include Uddin et al. [19] and Dairay et al. [16]. The experimental work of Lee and Lee [47] for $Re_D = 20\,000$ is also compared with the present LES.

Figure 12 shows the normalized Nu variation across the radial length of the impingement-wall. The present results agree with the previous experimental works. Grid-I substantially under predicts the value of Nu beyond $r/D > 1.5$ with the secondary Nu peak being clearly absent. Increased azimuthal and radial resolution (Grid-II) resulted in a significant improvement in the prediction of the Nu number profile. However, the secondary peak was significantly under-predicted with only a modest hint of the peak at $r/D = 2.1$. Grid-III has the best agreement predicting both the primary and secondary Nu peaks. The local minimum is observed at $r/D \approx 1.5$ and a secondary peak at $r/D \approx 2.0$ consistent with the earlier observations in literature for similar configurations. For $r/D > 2.0$, the Nusselt number decreases monotonically.

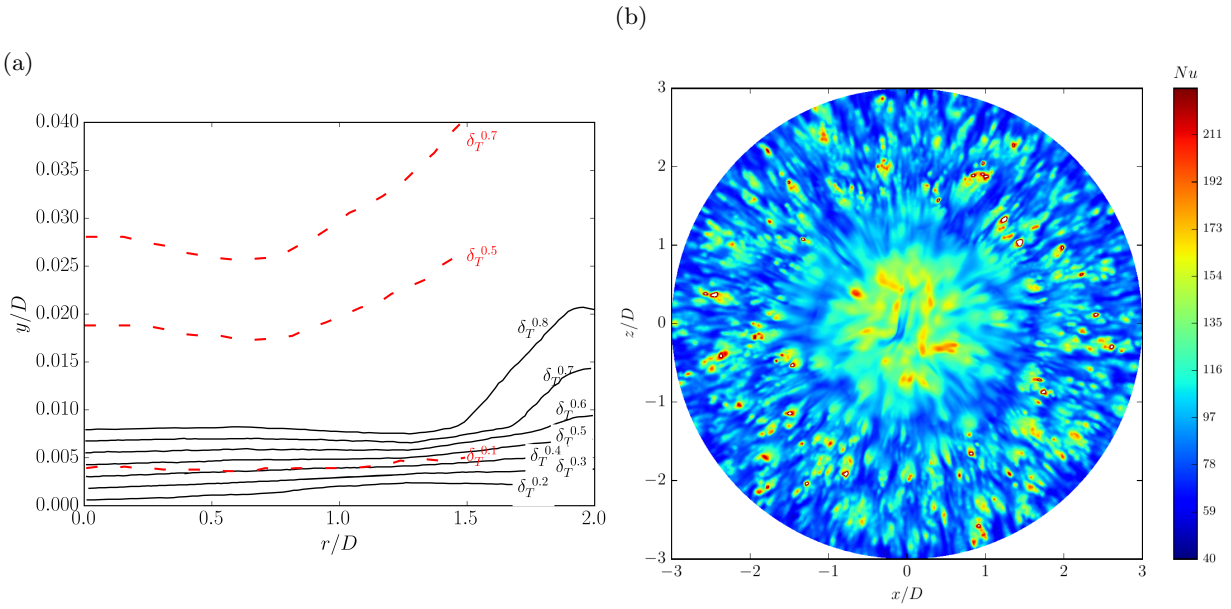

Figure 13: (a) Contours of thermal boundary layer thickness factor δ_T^α in the near-wall region; ——: present LES at $Re_D = 23\,000$; - - - -: laminar DNS data of Rohlfs et al. [17] at $Re_D = 1804$, $h/D = 4.5$, and (b) visualization of the jet-impingement wall at $Re_D = 23\,000$ with contours of instantaneous Nusselt number.

To visualize the near-wall thermal behaviour, a thermal boundary layer thickness factor denoted δ_T^α is used as the thickness at which the fluid temperature near-wall attains a certain fraction of the characteristic local temperature difference as described by Rohlfs et al. [17]. The definition of α is given as

$$\alpha = \frac{T_w(r) - T_f(r,y)}{T_w(r) - T_{ref}} \tag{8}$$

where T_w is the impingement-wall temperature, T_f is the fluid temperature and T_{ref} is the reference temperature. The levels of δ_T^α are shown in figure 13(a). The thermal boundary layer thickness is relatively thin when compared to a laminar jet (see Rohlfs et al. [17]) which is evident since the momentum of the fluid in the present case is higher, causing higher advection and thereby restricting the growth of the thermal boundary layer. A local thinning of the boundary layer is observed between $r/D = 1.0$ to 1.5 where the local acceleration of the fluid has also been observed to be a maximum. Beyond $r/D = 1.75$, the boundary layer begins to develop. The instantaneous distribution of the Nusselt number is shown in figure 13(b). The maximum normalized Nu is found in the stagnation region and the 'hot', and 'cold' spots are visualized side by side along the radial wall-jet region as proposed by Uddin et al. [19]. These could be appearing due to the local unsteady flow separation and reattachment resulting in the increase and decrease of local temperatures.

Overall, the dynamics under jet-impingement, both fluid flow and heat transfer characteristics are satisfactorily reproduced by comparison with representative experimental and numerical studies. The LES results from the analysed configuration agree favourably and are deemed suitable for capturing the flow features of the impinging-jet.

4 Vibrating-wall circular jet-impingement configuration (VWJ)

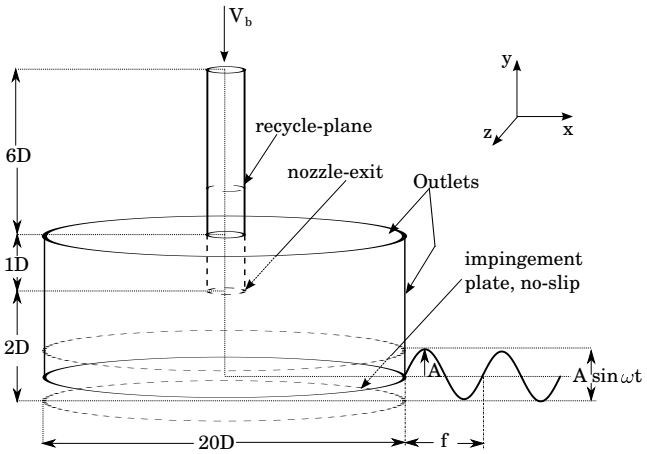

Figure 14: Schematic representation of the baseline vibrating-wall circular jet impingement configuration along with the boundary conditions and the coordinate system used for the simulations.

The baseline simulation of a turbulent vibrating-wall circular jet-impingement configuration is now presented. A schematic representation of the configuration along with the boundary conditions is shown in figure 14. The following investigations of the baseline vibrating-wall circular jet-impingement configuration are for a Re_D of 23 000 with a mean nozzle-to-wall distance of $1.75D$ with the wall motion within the region of $0 \leq y/D \leq 0.5$ with $y/D = 2$ at the nozzle-exit and a vibration frequency of 100 Hz.

Grid-III, the configuration that produced accurate results in the grid-sensitivity study of the static-wall jet-impingement is employed herein with relevant changes to the boundary conditions to accommodate mesh motion. The code was modified so that Equations 1, 2, 6 coupled with the mesh displacement equation (Equation 9), are solved concurrently. For the present cases, the mesh points are explicitly specified through the mesh displacement equation. The motion of the impingement wall is defined by,

$$\Delta \mathbf{S} = A \sin(\omega t) \tag{9}$$

where $\omega = 2\pi/T$ is the angular frequency, A, the displacement amplitude and T the time period of vibration. The predefined mesh motion is prescribed by a moving wall boundary condition implemented as a Dirichlet boundary condition. This boundary condition adjusts the flux due to mesh motion. The total flux, ϕ, through the moving wall is maintained at zero by updating the wall-normal velocity component to the corresponding mesh motion. Additionally, the motion velocity is calculated from the volume swept by a face in motion. In the present moving boundary method, the mesh undergoes deformation without undergoing a change in the number and connectivity of the hexahedral control volumes. The control volumes essentially expand and contract to achieve the enforced amplitude of mesh deformation[48]. The mesh motion is achieved by direct displacement of the nodes supporting the mesh while preserving the mesh quality. The coordinate system followed is similar to that of the SWJ in §3.2. It is important that the mesh at its fully expanded state before compression has a sufficiently high spatial resolution to capture the associated turbulent length scales to bound the local cell Reynolds number. As a result, the mesh at the completely compressed phase leads to tight constraints on the time-step. Accordingly, the mesh movement was restricted to between $y/D = 0$ and 0.5 with $0.25D$ as the amplitude. All the boundary conditions are similar to that of the SWJ, excluding those of the impingement wall. The wall is set as a moving boundary with a constant heat flux condition for temperature. The amplitude to nozzle-to-wall distance ratio, ζ is 0.14. The simulations are initialized with the LES of the SWJ from §3.2.

4.1 Results (Vibrating-wall circular jet-impingement configuration)

4.1.1 Fluid dynamics

Before analysing the unsteady flow features, it is useful to have an insight to the overall flow field within the domain as a result of the impingement-wall vibration. The flow dynamics experience change compared to the conventional flow regimes of a SWJ, due to the periodic mechanical interaction of the wall with the

free-jet at varying nozzle-to-wall distances. Figure 15(a) shows the time-mean and phase-averaged results of the SWJ and the VWJ, compared at different axial distances from the nozzle-exit along the radial direction.

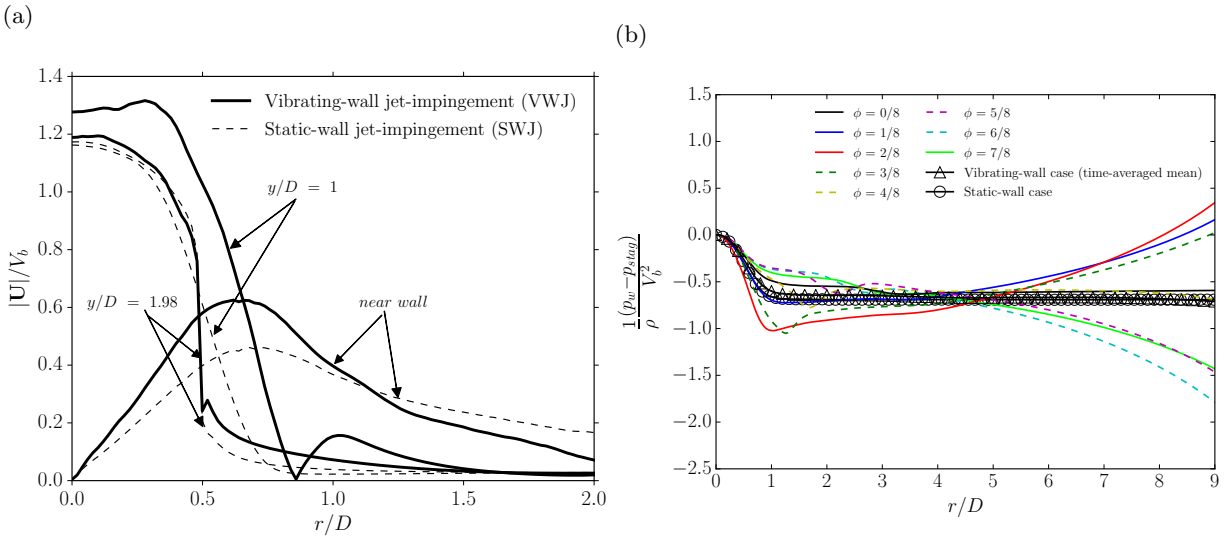

Figure 15: (a) Time-mean (SWJ) and phase-averaged (VWJ) velocity magnitude, $|\mathbf{U}|$ normalized by the bulk velocity V_b as a function of radial distance r/D at axial locations, $y/D = 1.98$, 1 and near-wall. ——: present LES result of the VWJ at $Re_D = 23\,000$; - - - -: present LES result of the SWJ at $Re_D = 23\,000$, and (b) wall pressure as a function of radial location. ——: present LES result of the VWJ during upward movement of the wall; - - - -: during downward movement of the wall; solid line with symbols: Static wall case.

In figure 15(a), the impingement-wall of the VWJ is at its maximum positive displacement, having moved to $y/D = 0.5$ from 0. The normalized time-mean and phase-averaged velocity profiles close to the nozzle-exit closely overlap each other, which shows that in regions close to the nozzle-exit ($y/D = 1.98$), the impact of wall motion for the VWJ is negligible. However, on closer inspection, a short spike at $r/D = 0.5$ is observed for the VWJ which is at the nozzle boundary edge where the fluid is in contact with the quiescent fluid domain and, as a consequence of the wall motion, the pressure imparted affects the fluid immediately upon exit. On moving further downstream of the nozzle-exit, at $y/D = 1$, the effect of the positive displacement of the wall is observed as a marked increase in the mean velocity. Additionally, there is a translocation in the curve of the VWJ $\approx 0.2D$ indicating that the free-jet at $y/D = 1$ has expanded in the radial direction. At the near-wall region, the increased velocity is seen until about $1D$ however, the velocity of the VWJ decays faster than its static-wall counterpart.

Figure 15(b) shows the pressure profiles on the wall for the static and vibrating wall cases at different phases of wall motion. The typical Gaussian profile is retained for the static wall case. Due to high static pressure in the stagnation region, the favourable pressure gradient drives the flow in the radial direction leading to the formation of the wall-jet. However, for the vibrating case, this characteristic Gaussian profile is altered due to the wall motion. Due to the sinusoidal variation in the movement of the impingement surface, a wider spread in the pressure distribution is seen. During the upward movement of the wall ($\phi =$ 0/8, 1/8, 2/8), the gradient is high in the stagnation region meaning the velocity is substantially higher in the stagnation region compared to the rest of the domain. The increased shear and velocity are seen until about $r/D = 4.5$ and then the gradient gradually decreases which is seen as a decrease in the velocity of the wall-jet beyond the stagnation zone. During the downward movement of the wall ($\phi = 3/8$, 4/8, 5/8, 6/8), the gradient is higher beyond the stagnation zone where velocity increase is observed.

Figures 15(a) and (b) clearly indicate that the impingement-wall vibration has an impact on the mean flow field, and thus requires a more detailed analysis. Phase-averaged/ensemble-averaged information along the required phases of the sinusoidal impingement-wall motion is useful in giving a general insight into the flow field. Therefore, the frequencies of the system need to be analysed since it is necessary to choose the right time scales for observation and ensemble-averaging in a system undergoing periodic change. The frequency characteristics of a system are represented by the Strouhal number defined as $St = fL/U$, where L and U are the length and velocity scales respectively. However, the choice of the length scale is not straight forward since it varies due to the induced vibration. The dimensionless parameter $F = fA/V_b$, which is a modification of the Strouhal number is used following Wen [5] which relates the vibrational frequency, f and the amplitude of vibration, A.

(a)

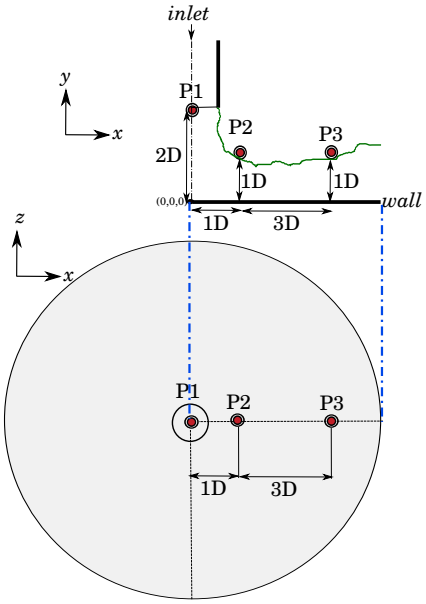

(b)

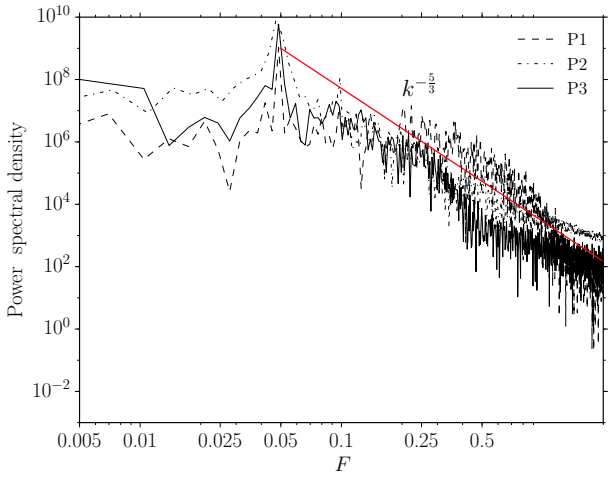

Figure 16: (a) Schematic representation of the domain in x-y and x-z planes showing the location of the diagnostic points used for recording velocity signals, and (b) power spectral density as a function of dimensionless parameter F for the recorded instantaneous velocity signals in the domain. - - - -: Point-1; $-\cdot-\cdot-$: Point-2; ——: Point-3.

The intrinsic time scales of the observation or ensemble-averaging have to be less than or equal to the time scales of flow. In the present configuration, the observed frequency of the flow field f_{jet} has to be lower than or equal to the wall vibration frequency, f, to enable the use of the period of wall vibration as the preferred time scale of observation. Diagnostic points were placed at different locations in the domain of the VWJ as shown in figure 16(a) to acquire instantaneous velocity signals at every time-step. Point–1 (P1) was located close to the nozzle-exit (at $y/D = 1.98$ and $r/D = 0$) to verify whether the wall vibration influences close to the inlet, Point–2 (P2) was located in the shear layer (at $y/D = 1.0$ and $r/D = 1.0$) and Point–3 (P3) was located further away from the stagnation region (at $y/D = 1.0$ and $r/D = 4.0$) and into the wall-jet.

The power spectral density of the acquired signals are plotted against the dimensionless parameter F in figure 16(b). All the digitized points exhibit a peak at $F = 0.049$ that correspond to a frequency of 100 Hz. Since the applied frequency of wall-vibration ($f = 100$ Hz) is the dominant frequency in the flow field, the vibrational time scale is preferred for the ensemble-averaging. Data acquisition is performed for 8 phases or wall positions in one period of vibration. The phase-averaging is carried out for typically over 15 periods of wall-vibration. The phase-averaged results are presented as phases, $\phi = 0/8$ through $7/8$.

4.1.2 Phase-averaged statistics

The phase-averaged statistics are presented for all the phases ($\phi = 0 - 7/8$) of the impingement-wall motion. The phase, $\phi = 0/8$ corresponds to the impingement-wall position at $y/D = 0.25$, displaces vertically upward attaining the maximum positive displacement at $\phi = 2/8$ ($y/D = 0.5$). The impingement-wall descends through phases, $\phi = 3/8$, $4/8$ and $5/8$ before reaching the phase, $\phi = 6/8$ corresponding to the maximum negative displacement ($y/D = 0$). At $\phi = 6/8$, the VWJ resembles the configuration of the SWJ having a similar nozzle-to-wall spacing of $2D$. Thus, the comparisons with the SWJ are made for this phase alone, and the SWJ results are indicated by dashed lines if presented. The individual phase is indicated at the top of each sub-plot and a marker showing the position of the impingement-wall on one vibration period is also shown.

The profiles of phase-averaged mean centreline ($r/D = 0$) axial velocity normalized by the bulk velocity is shown in figure 17(a). During the positive displacement of the wall, a negative velocity is seen close to the impingement-wall, unlike the SWJ due to the moving wall contacting the potential jet core. Though the jet core is not likely to be completely formed under the present condition where the nozzle-to-wall spacing is less than $2D$, and induced wall motion shortening the potential core length even further, the centreline

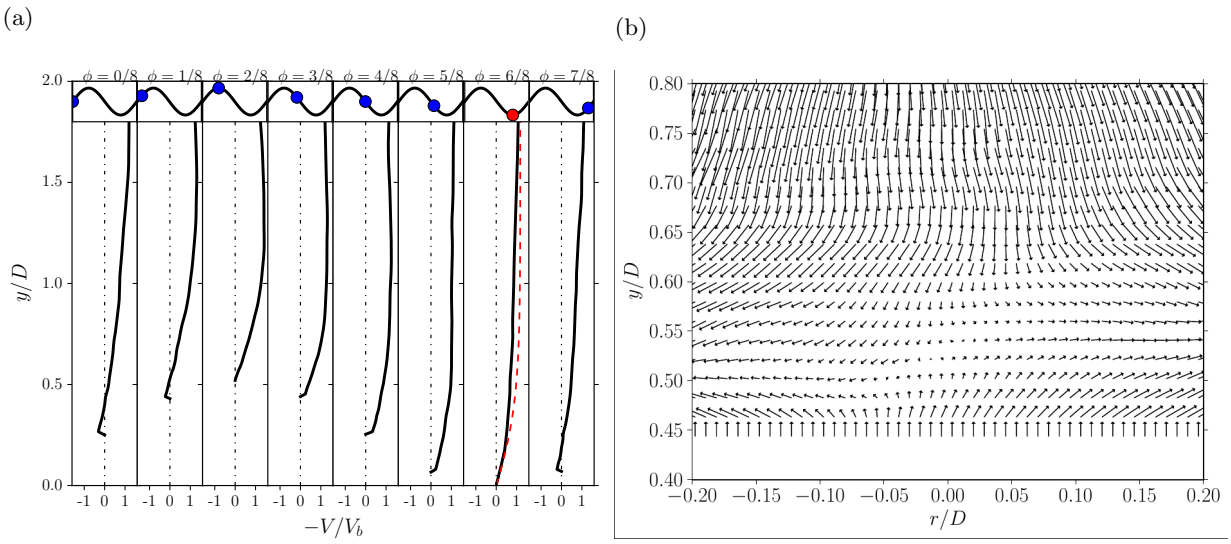

Figure 17: (a) Phase-averaged mean axial velocity V normalized by the bulk velocity V_b at $r/D = 0$ for phases $\phi = 0/8$ through $7/8$. ——: present LES result of the VWJ at $Re_D = 23\,000$; - - - -: present LES result of the SWJ at $Re_D = 23\,000$; ●: location of the impingement wall in a period of vibration, and (b) visualization of instantaneous near-wall velocity vectors for the present LES of the VWJ at $Re_D = 23\,000$ and at phase, $\phi = 1/8$, showing reverse flow at $y/D \approx 0.45$-0.55.

axial velocity is clearly affected causing a change in the point of inflection. Since the distance required for the jet core to develop is restricted, all the momentum from the jet is imparted to the wall. This can be seen in the velocity vectors as shown in figure 17(b). The map of velocity vectors in the stagnation region is shown for the VWJ at $\phi = 1/8$ where the vectors are convected away radially and axially from the wall. Reverse flow is seen up to axial distance of $y/D = 0.55D$ for the region between $r/D \pm 0.1$.

As the impingement wall traverses vertically to the maximum positive displacement at phase, $\phi = 2/8$, the change in the point of inflection on the mean axial velocity curve disappears as no further energy from the wall is imparted into the free-jet. When the impingement wall descends ($\phi = 3/8$, $4/8$, $5/8$), the curvature is retained back to the conventional shape. This reappears at phase, $\phi = 7/8$ since the impingement wall begins to displace positively again. This interactive effect is greatest in the jet core where the maximum opposition to the jet occurs. Moving radially downstream from the stagnation region ($> r/D \approx 0.5$), this collision effect disappears as seen in figure 18.

The fluid accelerates after impingement and spreads radially leading to the formation of the wall-jet. At $r/D = 1$, the wall-jet has its maximum speed in the near-wall region during the positive displacement of the impingement wall as shown in figure 18. However, due to viscous effects, there is a phase lag, and the maximum velocity occurs at $\phi = 3/8$ as opposed to $\phi = 2/8$. The maximum velocity then decreases upon the descent of the wall owing to mass conservation. It is interesting to note that the velocity magnitude for the SWJ is higher than that of the VWJ. This is because the point of comparison is made at the lowest point of the vibrating impingement-wall stroke. Instead of the mean position, $y/D = 0.25$, the maximum speed of the SWJ lies between the values for the upstream and downstream strokes. The high local velocity created at the beginning of the wall-jet gains no further momentum and starts to decay as the wall descends. The time scales of the vibration are much higher compared to the flow time scales, thus, the generated high velocity of the wall-jet is seen to reduce as the impingement-wall approaches its lowest point, at $y/D = 0$.

The above holds until the radial distance of $r/D = 2.0$ (figure 18b). The phenomenon of velocity increase upon ascent and decrease or compensation during descent is altered on moving radially downstream into the wall-jet region. The maximum velocity in the wall-jet now occurs when $\phi = 5/8$ at $r/D = 2.0$ and when $\phi = 6/8$ at $r/D = 2.5$. The increased local acceleration of the fluid from $r/D < 1$ is realized at different phases of the wall motion at differing radial locations. At $r/D = 2.5$ (figure 18c), the velocity of the VWJ ($\phi = 6/8$) is higher compared to the SWJ. Because of the variation in the time scales, the effect or the decay of the increased local acceleration is observed after the wall begins to descend, thus creating a higher wall-jet velocity at distances beyond $r/D = 2.0$ (figure 18c). However, the maximum velocity for both the SWJ and VWJ are at the radial location $r/D = 1$.

The phase-averaged r.m.s of the radial velocity fluctuations at $r/D = 1.5$ and 2.5 are presented in

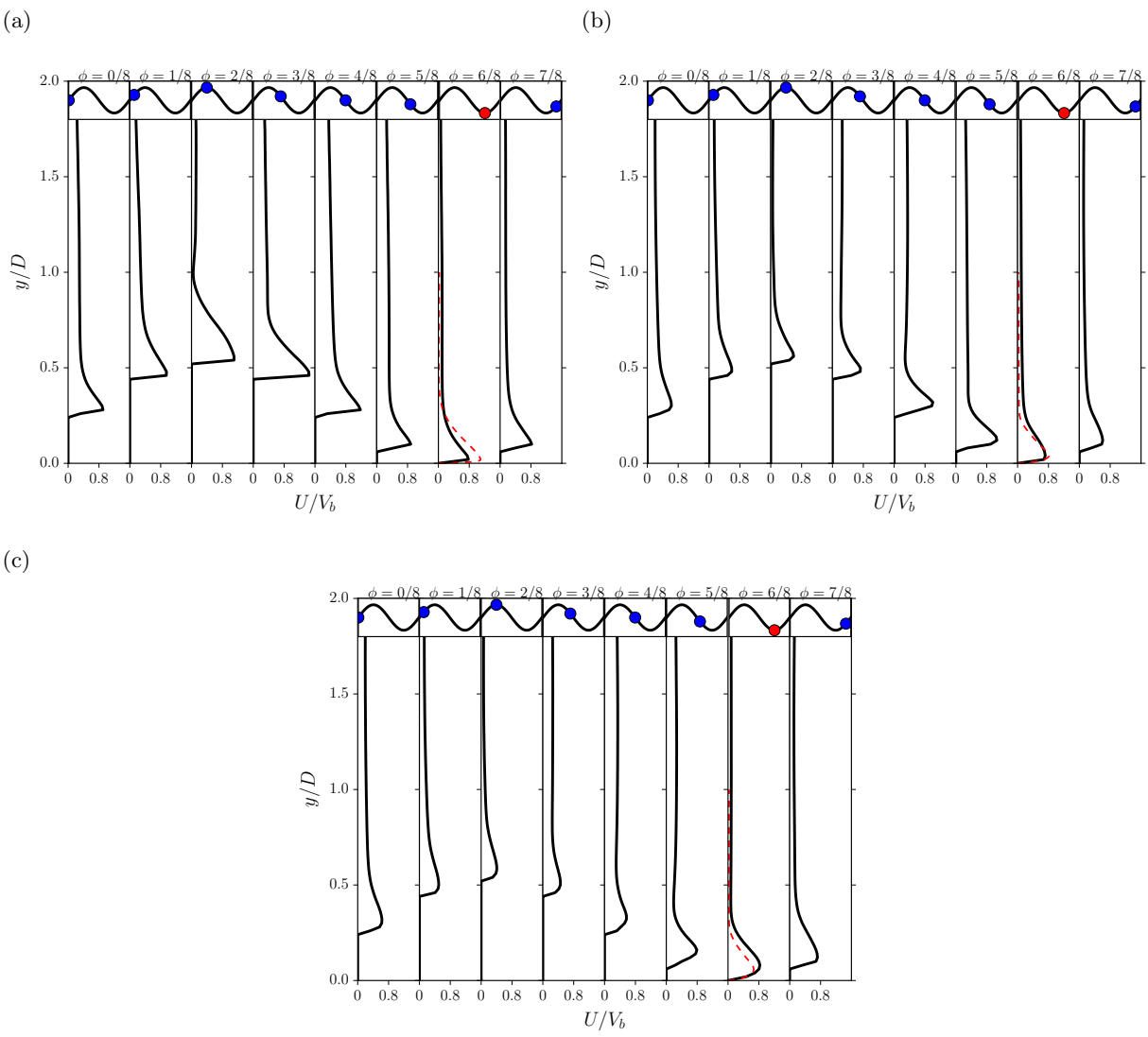

Figure 18: Phase-averaged mean radial velocity U normalized by the bulk velocity V_b at (a) $r/D = 1.0$, (b) $r/D = 2.0$, and (c) $r/D = 2.5$ for phases $\phi = 0/8$ through $7/8$. ——: present LES result of the VWJ at $Re_D = 23\,000$; - - - -: present LES result of the SWJ at $Re_D = 23\,000$; ●: location of the impingement wall in a period of vibration.

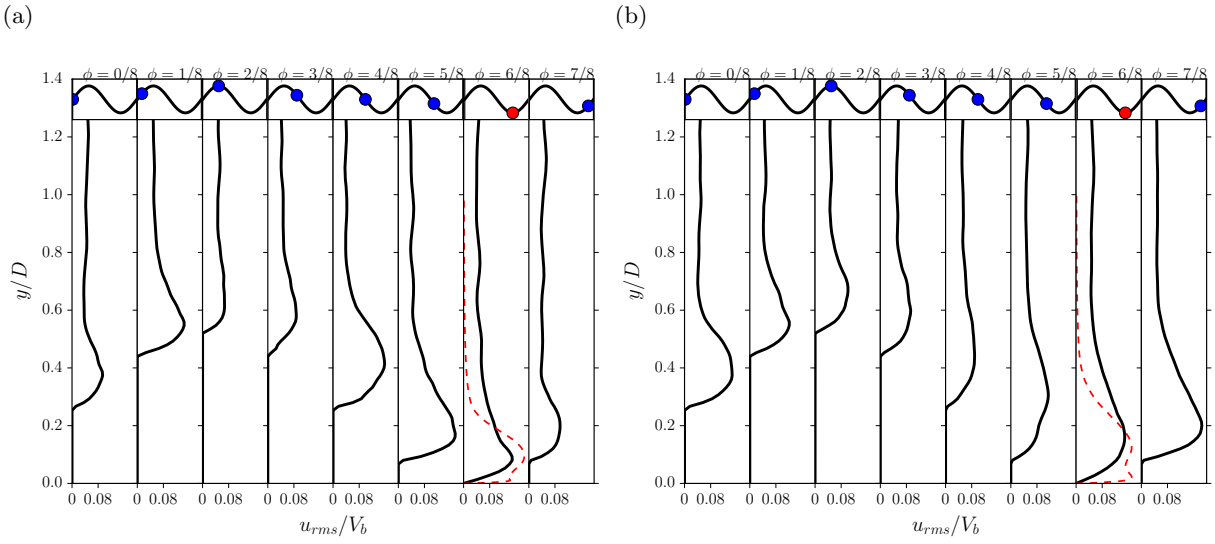

Figure 19: Root mean square of radial velocity u_{rms} normalized by the bulk velocity V_b (a) at $r/D = 1.5$ (b) at $r/D = 2.5$ for phases $\phi = 0/8$ through $7/8$. ——: present LES result of the VWJ at $Re_D = 23\,000$; - - - -: present LES result of the SWJ at $Re_D = 23\,000$; ●: location of the impingement wall in a period of vibration.

figure 19 (a) and (b) respectively. The radial u_{rms} values exhibit the influence of wall motion very strikingly with an increase in the level of r.m.s velocities across the wall-normal direction. This increase is even noticeable on moving radially downstream from the stagnation region. The effect of wall motion influences the velocity fluctuations in the axial direction beyond $0.4D$ from the wall that is not seen in the case of a SWJ. These increased radial fluctuation levels characterize the unsteadiness brought about by the meandering jet as a result of wall motion. The characteristic double peaks seen in the SWJ are no longer observed in the VWJ.

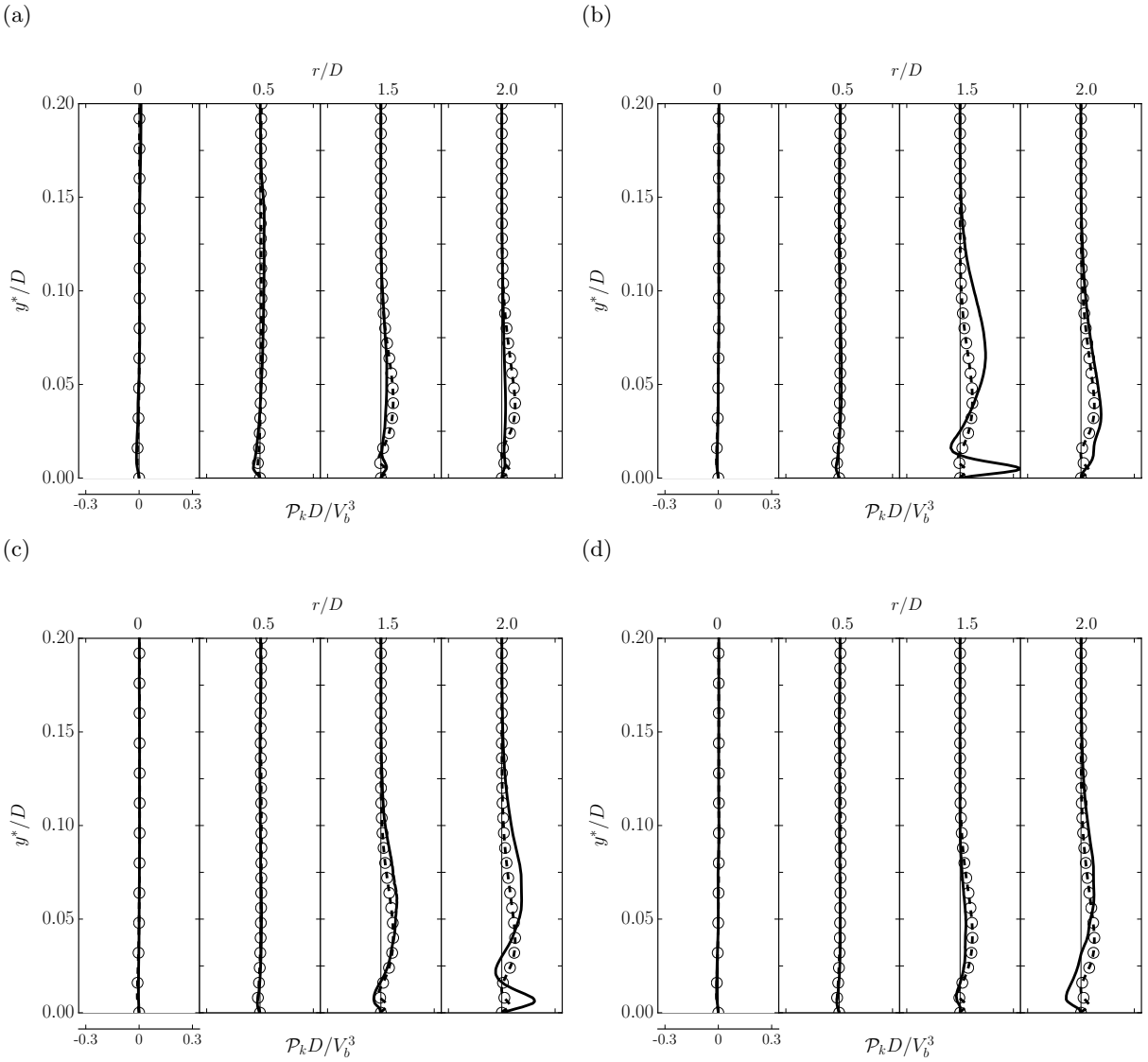

Figure 20: Production of Turbulence kinetic energy at different radial locations during phases of wall motion (a) ϕ = 2/8 (b) ϕ = 4/8 (c) ϕ = 5/8 and, (d) ϕ = 6/8 compared with the present LES of static wall case (dashed line with open symbols).

The turbulence production is shown for phases ϕ = 2/8, 4/8, 5/8 and 6/8 in figure 20. The results are compared with the static wall case results at the same radial locations. The acceleration and deceleration of the wall-jet reflected as an increase and decrease in the turbulence production is seen. The maximum turbulence production is almost twice that of the static wall case at $r/D = 1.5$ (at $\phi = 4/8$) while the near wall peak becomes even stronger in the vibrating case. This is due to the high shear caused by the flow, and the moving wall adds energy to the mean flow. It is also interesting to note that this maximum appears at the same radial location for both static and vibrating cases. The viscous diffusion term ($\mathcal{D}_k$) was very low and did not undergo any significant changes; hence this data is not included.

4.1.3 Vortical structures and heat transfer

The thermal signatures on the impingement wall are discussed using Nusselt number profiles. The phase-averaged Nusselt number, Nu_ϕ is given as,

$$Nu_\phi = \int_0^t \frac{1}{\Delta t} Nu(\phi, t) dt \tag{10}$$

where ϕ represents the phase of the wall motion for which averaging was performed. The time-averaged Nusselt number, Nu_{avg} is derived to quantify the total effect of the impingement wall vibration on heat transfer and hence averaged over all the phases and is given as,

$$Nu_{avg} = \int_0^\phi \frac{1}{\Delta \phi} \int_0^t Nu(\phi, t) dt d\phi \tag{11}$$

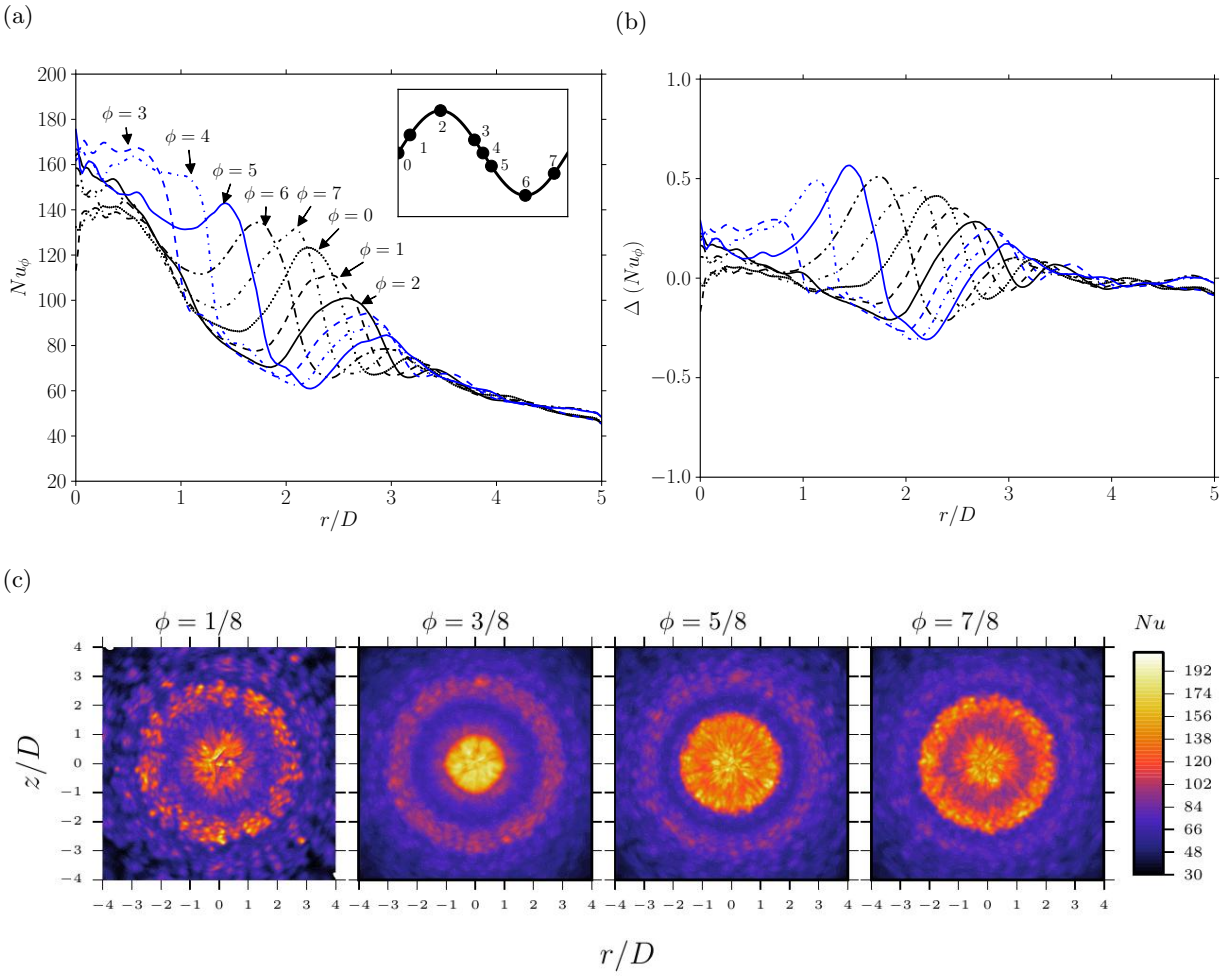

Figure 21: (a) Phase-averaged Nusselt number Nu_ϕ on the impingement wall of the VWJ as a function of radial distance r/D for phases, $\phi = 0/8$ through 7/8. $\cdots$:$\phi = 0/8$; - - - -: $\phi = 1/8$; ——: $\phi = 2/8$; - - - - (blue): $\phi = 3/8$; $-\cdot-\cdot-$ (blue): $\phi = 4/8$; —— (blue): $\phi = 5/8$; $-\cdots-$: $\phi = 6/8$; $-\cdot-\cdot-$: $\phi = 7/8$; ●(inset): location of the impingement wall in a period of vibration and the corresponding numbers indicating phases, (b) Phase-averaged Nusselt number ratio $\Delta(Nu_\phi)$ as function of radial distance r/D for the VWJ at $Re_D = 23\,000$ for phases $\phi = 0/8$ through 7/8. (for legend refer figure 21a), and (c) visualization of the jet-impingement wall for the VWJ at $Re_D = 23\,000$ with contours of intantaneous Nusselt number Nu for phases $\phi = 1$, 3, 5 and 7/8.

The phase-averaged Nusselt number profiles on the impingement wall for the VWJ are shown in figure 21(a) at phases, $\phi = 0/8$ through 7/8. The figure shows the unsteadiness in the flow field through the range of Nu_ϕ vibrations observed at each phase ϕ. However, the spread of the oscillations narrows with increasing radial distance and at $r/D = 3.0$, the fluctuation levels among the phases fall within $\pm 1\%$ indicating that the wall vibration effects become negligible beyond this radial distance. With the region of interest $r/D < 3.0$, two striking features are observed. First, at the stagnation region, increased rate of

heat transfer is observed only after the wall has reached its maximum positive displacement and begun to descend. This region is highly phase time-dependent as there is constant change in the momentum of the fluid impacting the wall. Secondly, periodic shifts in the location of the secondary maximum of Nusselt number are observed. As the wall moves upwards, the secondary Nusselt number peak moves radially outward. The location of the peak is related to the large vortical structures seen in figure 22. The location of the dominant vortical structures matches the location of the secondary Nu peaks. Due to the radial fluid acceleration, the vortical structures create a strong shear on the impingement wall resulting in a wall renewal effect causing an increase in local heat transfer.

As the impingement wall undergoes positive displacement in the wall-normal direction, it is in contact with the primary vortices generated due to the shear between the free-jet and the quiescent fluid. The flow upon impingement moves downstream interacting unsteadily with the wall resulting in the formation of the secondary vortices. As the wall undergoes a negative displacement, the time scales are such that the formed primary and secondary vortices move radially downstream altering the radial location of the secondary Nu peak. Because of the impingement wall motion and the relative velocity of the wall imparting additional acceleration to the fluid, the strength and location of the secondary vortices are affected which is seen as increase and decrease in the peak value of the secondary Nusselt number peak. As the secondary vortex moves along the radial direction, the secondary vortex removes the heat from the wall and in the process enables the inflow of colder fluid and therefore increasing the thermal boundary layer thickness upstream of the secondary vortex and hence a dip before the outer Nusselt peak.

Figure 21b shows the variations in heat transfer relative to the SWJ, visualized by using ΔNu_ϕ, given by the expression $\Delta Nu_\phi = (Nu_\phi - Nu_{swj})/Nu_{swj}$ where Nu_ϕ is the phase-averaged Nu and Nu_{swj} is the time-mean Nu for the static-wall jet-impingement configuration from §3.2. Enhancement in heat transfer seen as positive values of ΔNu_ϕ experience a maximum at $\phi = 5/8$ due to the SWJ experiencing the dip before its corresponding secondary Nu peak at the same location. The enhancement in heat transfer of the VWJ within the region $r/D \leq 2$ reaches up to 45% compared to the SWJ. However, after this radial distance there is a substantial drop in the heat transfer rate; This is up to 40% in the heat transfer rate at phase, $\phi = 6/8$ of the wall. It is also interesting to note that the peak heat transfer rates which are higher than those of the SWJ occur during the downward displacement of the wall.

Maps of instantaneous Nusselt number are shown in figure 21(c) for different phases. Maximum heat transfer within the region $r/D \leq 1$ occurs at $\phi = 3/8$; this is after the maximum displacement ($\phi = 2/8$) because of the momentum lag due to viscous effects (discussed in §4.1.2). Since the nozzle-to-wall spacing is reduced during the vibrating period, the momentum imparted by the fluid on the wall is also maximum. During the negative displacement, at $\phi = 5/8$, the momentarily accumulated fluid due to the previously traversed phases, coalesce, and increase the radial distance to which the heat removal is enhanced. Although the maximum Nu at this phase is lower in the stagnation region compared to $\phi = 3/8$, the region of increased Nu expands radially to $r/D \leq 1.5$. After the impingement wall has reached its lowest point and begun to displace positively, at $\phi = 7/8$, the intensity of the Nu in the stagnation region weakens further. These mechanisms are reflected in figure 21(a) where increased Nu is seen in regions closer to the stagnation region during the positive displacement.

Figure 22 shows the effect of wall movement on turbulence in the near wall region. In each figure, the top panel shows the vortical structures represented as contours of vorticity magnitude, $(\sqrt{\omega_i\omega_i})$, of the instantaneous velocity field and center panel shows the corresponding Nusselt number distribution and the bottom panel shows the phase-averaged radial Nusselt number. Dashed red lines at radial locations $r/D = 1.5$ and 2.8 are used as markers to demonstrate the dynamics. It is clear from the figures that due to the wall movement, the near-wall vortical structures of high vorticity are accelerated in the radial direction and correspondingly increase the local Nusselt number causing the secondary Nusselt peak to move radially outward. As the vortical structures move outward, the magnitude of vorticity decreases and correspondingly the hot-spots and the Nusselt number intensity also decreases eventually seen as a decrease in the magnitude of the secondary Nusselt number peak.

The time-averaged Nusselt number, Nu_{avg} is shown in figure 23(a). It is observed that there is a marked improvement in the heat transfer up to $r/D = 1.5$ when compared to the static-wall jet-impingement case. The enhancement in heat-transfer is nearly 18% in the stagnation region for the vibrating wall case when compared to the static-wall configuration. The increase in heat transfer is compensated by the local unsteadiness created in the boundary layer and unsteady separation. However, this may vary from a reduction of impingement wall vibration frequencies and jet Reynolds numbers enabling smoother vortical sweeps and in turn increased heat transfer without undulation. It is also interesting to note that the amplitude of the secondary peak is decreased. Figure 23(a) also shows the range of the phase-averaged

(a) Phase, $\phi = 6/8$ (b) Phase, $\phi = 7/8$ (c) Phase, $\phi = 0/8$

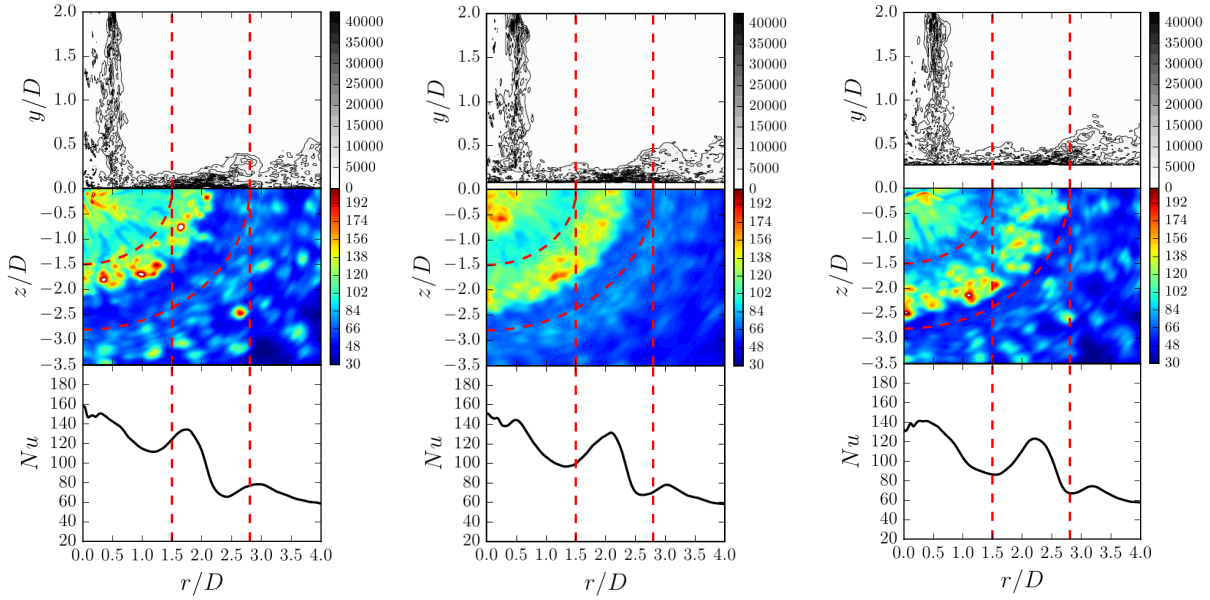

(d) Phase, $\phi = 1/8$ (e) Phase, $\phi = 2/8$ (f) Phase, $\phi = 3/8$

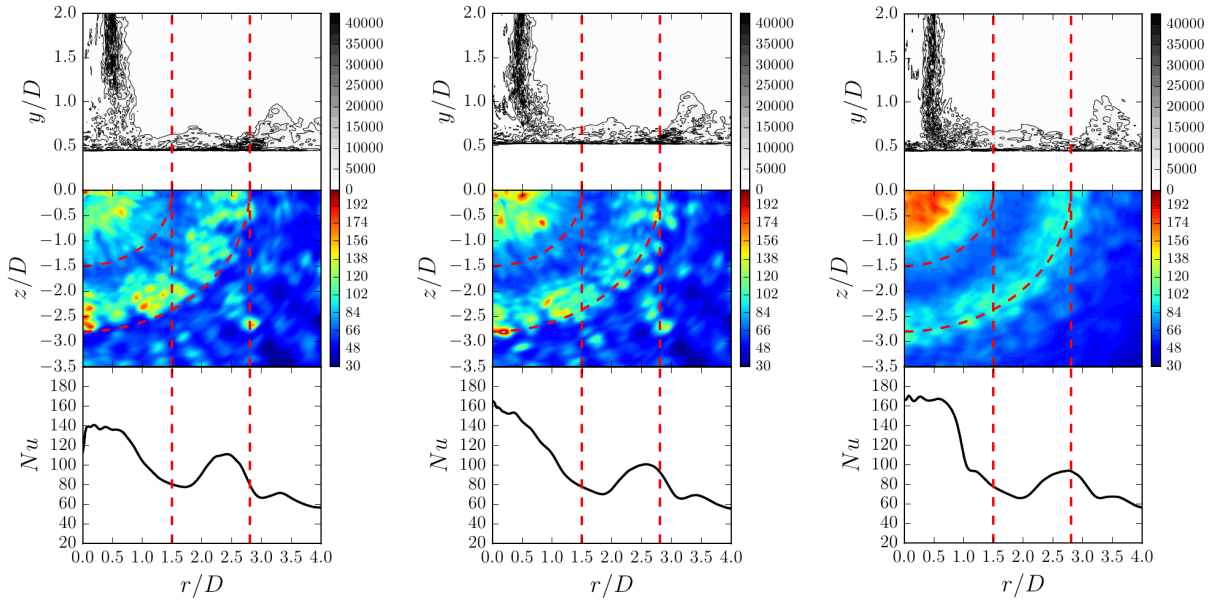

Figure 22: Visualization of the VWJ and the effect of wall movement on vortical structures and heat transfer at Re_D = 23 000 over a constant z plane with contours of instantaneous total vorticity magnitude, $(\omega_i\omega_i)^{0.5}$ (top panel), instantaneous Nusselt number distribution (center panel) and phase averaged Nusselt number (bottom panel) at phases, (a) $\phi = 6/8$ (b) $\phi = 0/8$ (c) $\phi = 1/8$ (d) $\phi = 2/8$ (e) $\phi = 4/8$ (f) $\phi = 5/8$. The vorticity contour levels are from 0 to 4.0×10^4 with increments of 5×10^3.

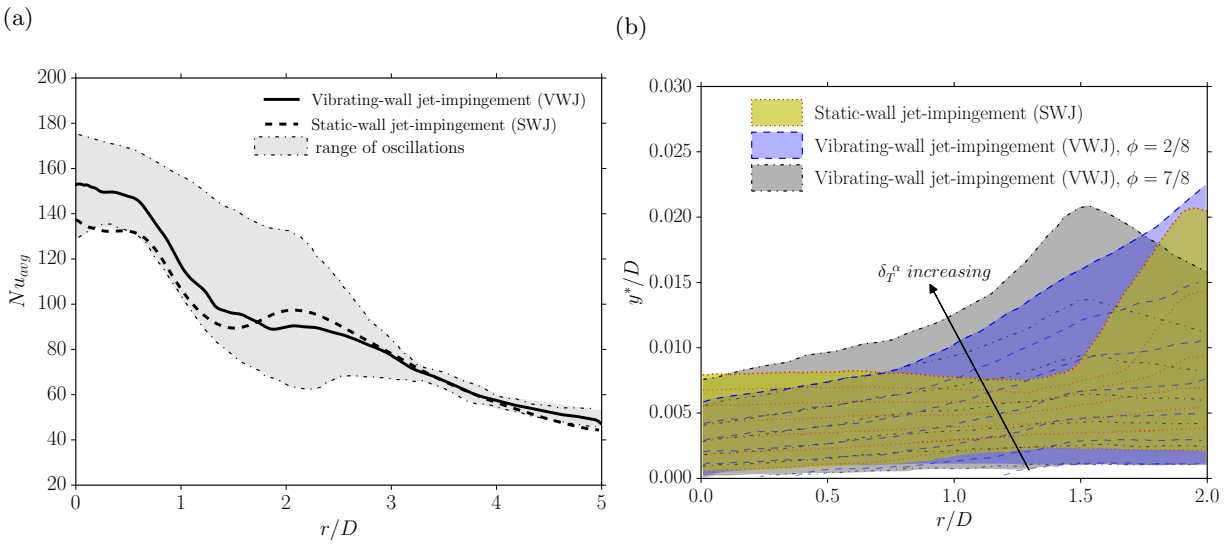

Figure 23: (a) Time-averaged Nusselt number Nu_{avg} on the impingement wall as a function of radial distance r/D. ——: present LES result for the VWJ at Re_D = 23 000; - - - -: present LES result for the SWJ at Re_D = 23 000; shaded region: range of oscillations of the phase-averaged Nusselt number Nu_ϕ from the present LES of the VWJ at Re_D = 23 000; and (b) visualization of the thermal boundary layer thickness factor $\delta_T{}^{\alpha}$ in the near-wall region for Re_D =23 000. $\cdots$: contours of $\delta_T{}^{\alpha}$ for the SWJ; - - - -: contours of $\delta_T{}^{\alpha}$ for the VWJ, $\phi = 2/8$; $-\cdot-\cdot-$: contours of $\delta_T{}^{\alpha}$ for the VWJ, $\phi = 7/8$; The contour levels of $\delta_T{}^{\alpha}$ are from 0.2 to 0.8 with increments of 0.1 (color shading for the sake of clarity).

Nu_ϕ oscillations.

The thermal boundary layer thickness map superimposed on the contours of $\delta_T{}^{\alpha}$ is shown in figure23(b). The thermal boundary layer thickness of the VWJ at $\phi = 2/8$ and $7/8$ are compared with the SWJ. The ordinate axis (y^*/D) represents the non-dimensional distance from the wall to enable the comparison of the thermal boundary layer thickness between the SWJ and VWJ configurations with the wall as the reference plane. The contour levels for α used for the map are from 0.2 to 0.8. At $r/D < 0.5$, the thermal boundary layer thickness reaches $\alpha = 0.8$ at approximately the same distance from the wall (≈ 0.0075) for ϕ=7/8 and the SWJ. At $\phi = 2/8$ (maximum positive displacement of the impingement wall), the thickness of the thermal boundary layer reduces further indicating the higher heat transfer rate in this region. However, the notable difference is in the growth of the boundary layer. The boundary layers for the VWJ ($\phi = 2/8$ and $7/8$) increase in thickness for lower radial distances as compared to the SWJ.

5 Conclusions

Large-eddy simulations of an incompressible turbulent circular jet impinging upon a vibrating heated wall supplied with a uniform heat flux have been performed at Re_D = 23 000. The mean nozzle-to-wall spacing is $y/D = 1.75$ with an impingement-wall vibration frequency, f = 100 Hz and an amplitude, $A = 0.25D$. A series of sub-systems were validated and then used to assemble the computational model of the vibrating-wall jet impingement configuration. In the process, the numerical methodology adopted has been critically examined with validations against previous experimental and numerical data.

The method of generating fully developed incompressible turbulent jet inflow using a recycled plane has been studied through LES of a turbulent pipe flow at Re_D = 24 600 and applied to both static-wall jet and vibrating-wall jet impingement configurations. The method preserved the flow structures and can be used in similar computational systems where a fully developed incompressible turbulent inflow is required. The baseline vibrating-wall configuration was established after validating the static vibrating-wall configuration.

Results for phase-averaged mean and fluctuating components have been presented at different phases within a period of the impingement-wall motion. Radial-flow velocity increase and decrease are found upon positive and negative displacement of the impingement wall respectively. However, this correlation changes with increases in the radial distance because of the viscous effects and beyond $r/D = 2.0$ increased velocity is seen during the negative displacement of the impingement wall. In the stagnation region, counterflow of the fluid is predicted due to the upward motion of the impingement-wall causing a change in the axial

velocity profiles. An increase in the turbulence kinetic energy production is seen and the maximum is almost twice that of the static wall case at $r/D = 1.5$.

The flow dynamics contribute to changes in the thermal imprints on the vibrating-wall impingement wall. The secondary maximum of the Nusselt number has been shown to be a strong function of the eddies present in the flow domain and it shifts radially based on the location and strength of these eddy structures. Large-eddies with no defined structure are convected away radially from the stagnation region during the positive displacement of the wall and are renewed close to the stagnation point during the negative displacement of the wall. This results in weaker convection in the wall jet and stronger stagnation heat transfer during the upstroke. As a result, the impingement-wall vibration affects the heat transfer only up to a radial distance $r/D = 3.0$. Beyond this radial distance, the dependence of Nu on radial distance is similar to that of a corresponding static-wall jet impingement configuration. Enhancement in heat-transfer is seen as an increase in the time-averaged Nusselt number (Nu_{avg}) up to a radial distance of $r/D = 1.5$ when compared to static-wall jet impingement. The enhancement in the stagnation region is about 18% when compared to the static-wall case. Apart from the moderate depreciation at $r/D = 2.0$, no further enhancement or depreciation of heat transfer is seen beyond this radial distance.

The present study has served to establish a computational model for a turbulent jet impinging upon a vibrating heated wall and then elucidate the dynamics of the system through the inter-relation between momentum and heat-transfer. This has generated a comprehensive set of results for one set of system parameters. This lays the foundation for the full parameter space to be explored so that optimum heat-transfer and possible control of the localised Nu peaks can be attained for practical applications. For the system parameters used to generate the present results, the high momentum of the jet means that the wall boundary layer is only moderately affected by the frequency and amplitude of the vibrating wall. Thus, wall vibration may have stronger effects when the momentum of the jet is relatively low. Accordingly, future investigations will map out the parameter space that combines jet Reynolds number (Re_D), the impingement-wall vibration frequency (f) and amplitude (A), and the stand-off distance between the jet exit and the impingement-wall.

Acknowledgements

Financial support from the Australian Research Council [ARC DP130103271] is gratefully acknowledged. This work was supported by resources provided by the Pawsey Supercomputing Centre with funding from the Australian Government and the Government of Western Australia.

References

[1] H. Martin, "Heat and mass transfer between impinging gas jets and solid surfaces," *Advances in Heat Transfer*, vol. 13, pp. 1–60, 1977.

[2] K. Jambunathan, E. Lai, M. A. Moss, and B. L. Button, "A review of heat transfer data for single circular jet impingement," *International Journal of Heat and Fluid Flow*, vol. 13, pp. 106–115, 1992.

[3] R. Viskanta, "Heat transfer to impinging isothermal gas and flame jets," *Experimental Thermal and Fluid Science*, vol. 6, pp. 111–134, 1993.

[4] K. Ichimiya and Y. Yoshida, "Oscillation Effect of Impingement Surface on Two-Dimensional Impingement Heat Transfer," *Journal of Heat Transfer*, vol. 131, no. 1, p. 011701, 2009.

[5] M.-Y. Wen, "Flow structures and heat transfer of swirling jet impinging on a flat surface with micro-vibrations," *International Journal of Heat and Mass Transfer*, vol. 48, pp. 545–560, Jan. 2005.

[6] D. Cooper, D. Jackson, B. Launder, and G. Liao, "Impinging jet studies for turbulence model assessment—I. Flow-field experiments," *International Journal of Heat and Mass Transfer*, vol. 36, pp. 2675–2684, July 1993.

[7] T. J. Craft, L. J. W. Graham, and B. E. Launder, "Impinging jet studies for turbulence model assessment—II. An examination of the performance of four turbulence models," *International Journal of Heat and Mass Transfer*, vol. 36, pp. 2685–2697, 1993.

[8] T. Craft, H. Iacovides, and J. Yoon, "Progress in the use of non-linear two-equation models in the computation of convective heat-transfer in impinging and separated flows," *Flow, Turbulence and Combustion*, vol. 63, no. 1-4, pp. 59–80, 2000.

[9] J. W. Baughn and S. Shimizu, "Heat transfer measurements from a surface with uniform heat flux and an impinging jet," *Journal of Heat Transfer*, vol. 111, pp. 1096–1098, 1989.

[10] X. J. Yan and N. Saniei, "Heat transfer measurements from a flat plate to a swirling impinging jet," in *Proceedings of the 11th Heat Transfer Conference Vol. 5*, vol. 5, pp. 497–502, 1998.

[11] V. Katti and S. V. Prabhu, "Experimental study and theoretical analysis of local heat transfer distribution between smooth flat surface and impinging air jet from a circular straight pipe nozzle," *International Journal of Heat and Mass Transfer*, vol. 51, pp. 4480–4495, 2008.

[12] M. Bovo and L. Davidson, "On the numerical modeling of impinging jets heat transfer—a practical approach," *Numerical Heat Transfer, Part A*, vol. 64, no. 4, pp. 290–316, 2013.

[13] R. Gardon and J. C. Akfirat, "The role of turbulence in determining the heat-transfer characteristics of impinging jets," *International Journal of Heat and Mass Transfer*, vol. 8, pp. 1261–1272, 1965.

[14] Y. M. Chung and K. H. Luo, "Unsteady Heat Transfer Analysis of an Impinging Jet," *Journal of Heat Transfer*, vol. 124, no. 6, p. 1039, 2002.

[15] Y. Chung, K. Luo, and N. Sandham, "Numerical study of momentum and heat transfer in unsteady impinging jets," *International Journal of Heat and Fluid Flow*, vol. 23, pp. 592–600, Oct. 2002.

[16] T. Dairay, V. Fortuné, E. Lamballais, and L.-E. Brizzi, "Direct numerical simulation of a turbulent jet impinging on a heated wall," *Journal of Fluid Mechanics*, vol. 764, pp. 362–394, 2015.

[17] W. Rohlfs, H. D. Haustein, O. Garbrecht, and R. Kneer, "Insights into the local heat transfer of a submerged impinging jet: Influence of local flow acceleration and vortex-wall interaction," *International Journal of Heat and Mass Transfer*, vol. 55, no. 25, pp. 7728–7736, 2012.

[18] M. J. Tummers, J. Jacobse, and S. G. J. Voorbrood, "Turbulent flow in the near field of a round impinging jet," *International Journal of Heat and Mass Transfer*, vol. 54, pp. 4939–4948, 2011.

[19] N. Uddin, S. O. Neumann, and B. Weigand, "LES simulations of an impinging jet: On the origin of the second peak in the Nusselt number distribution," *International Journal of Heat and Mass Transfer*, vol. 57, pp. 356–368, 2013.

[20] M. Hadžiabdić and K. Hanjalić, "Vortical structures and heat transfer in a round impinging jet," *Journal of Fluid Mechanics*, vol. 596, pp. 221–260, 2008.

[21] S. Roux, M. Fénot, G. Lalizel, L.-E. Brizzi, and E. Dorignac, "Experimental investigation of the flow and heat transfer of an impinging jet under acoustic excitation," *International Journal of Heat and Mass Transfer*, vol. 54, no. 15, pp. 3277–3290, 2011.

[22] A. Dewan, R. Dutta, and B. Srinivasan, "Recent trends in computation of turbulent jet impingement heat transfer," *Heat Transfer Engineering*, vol. 33, no. 4-5, pp. 447–460, 2012.

[23] M. Tsubokura, T. Kobayashi, N. Taniguchi, and W. Jones, "A numerical study on the eddy structures of impinging jets excited at the inlet," *International journal of heat and fluid flow*, vol. 24, no. 4, pp. 500–511, 2003.

[24] C. O. Popiel and O. Trass, "Visualization of a free and impinging round jet," *Experimental Thermal and Fluid Science*, vol. 4, no. 3, pp. 253–264, 1991.

[25] K. Ichimiya and S. Watanabe, "Numerical Analysis of a Two-Dimensional Jet Impinging on an Oscillated Heat Transfer Surface," *Journal of Heat Transfer*, vol. 131, no. 9, p. 094505, 2009.

[26] D. Klein and G. Hetsroni, "Enhancement of heat transfer coefficients by actuation against an impinging jet," *International Journal of Heat and Mass Transfer*, vol. 55, no. 15, pp. 4183–4194, 2012.

[27] M. Germano, U. Piomelli, P. Moin, and W. H. Cabot, "A dynamic subgrid-scale eddy viscosity model," *Physics of Fluids A: Fluid Dynamics (1989-1993)*, vol. 3, no. 7, pp. 1760–1765, 1991.

[28] D. K. Lilly, "A Proposed Modification of the Germano-Subgrid-Scale Closure Method," *Physics of Fluids A:Fluid Dynamics*, vol. 4, no. 3, pp. 633–635, 1992.

[29] C. Rhie and W. Chow, "Numerical study of the turbulent flow past an airfoil with trailing edge separation," *AIAA journal*, vol. 21, no. 11, pp. 1525–1532, 1983.

[30] F. Pellegrini and J. Roman, "Scotch: A software package for static mapping by dual recursive bipartitioning of process and architecture graphs," in *High-Performance Computing and Networking* (H. Liddell, A. Colbrook, B. Hertzberger, and P. Sloot, eds.), vol. 1067 of *Lecture Notes in Computer Science*, pp. 493–498, Springer Berlin Heidelberg, 1996.

[31] J. Den Toonder and F. Nieuwstadt, "Reynolds number effects in a turbulent pipe flow for low to moderate Re," *Physics of Fluids (1994-present)*, vol. 9, no. 11, pp. 3398–3409, 1997.

[32] G. Tabor and M. Baba-Ahmadi, "Inlet conditions for large eddy simulation: a review," *Computers & Fluids*, vol. 39, no. 4, pp. 553–567, 2010.

[33] J. W. Jewkes, Y. M. Chung, and P. W. Carpenter, "Modifications to a Turbulent Inflow Generation Method for Boundary-Layer Flows," *AIAA Journal*, vol. 49, pp. 247–250, Jan. 2011.

[34] M. Guala, S. Hommema, and R. Adrian, "Large-scale and very-large-scale motions in turbulent pipe flow," *Journal of Fluid Mechanics*, vol. 554, pp. 521–542, 2006.

[35] J. Morrison, B. McKeon, W. Jiang, and A. Smits, "Scaling of the streamwise velocity component in turbulent pipe flow," *Journal of Fluid Mechanics*, vol. 508, pp. 99–131, 2004.

[36] X. Wu and P. Moin, "A direct numerical simulation study on the mean velocity characteristics in turbulent pipe flow," *Journal of Fluid Mechanics*, vol. 608, pp. 81–112, 2008.

[37] J. Eggels, F. Unger, M. Weiss, J. Westerweel, R. Adrian, R. Friedrich, and F. Nieuwstadt, "Fully developed turbulent pipe flow: a comparison between direct numerical simulation and experiment," *Journal of Fluid Mechanics*, vol. 268, pp. 175–210, 1994.

[38] M. V. Zagarola and A. J. Smits, "Mean-flow scaling of turbulent pipe flow," *Journal of Fluid Mechanics*, vol. 373, pp. 33–79, 1998.

[39] C. Lawn, "The determination of the rate of dissipation in turbulent pipe flow," *Journal of Fluid Mechanics*, vol. 48, no. 03, pp. 477–505, 1971.

[40] L. F. Geers, M. J. Tummers, and K. Hanjalić, "Experimental investigation of impinging jet arrays," *Experiments in fluids*, vol. 36, no. 6, pp. 946–958, 2004.

[41] S. B. Pope, "Ten questions concerning the large-eddy simulation of turbulent flows," *New Journal of Physics*, vol. 6, pp. 35–35, Mar. 2004.

[42] I. B. Celik, Z. N. Cehreli, and I. Yavuz, "Index of resolution quality for large eddy simulations," *Journal of Fluids Engineering*, vol. 127, no. 5, pp. 949–958, 2005.

[43] T. Hällqvist, *Large eddy simulation of impinging jets with heat transfer*. PhD thesis, Royal Institute of Technology, Sweden, 2006.

[44] D. Lytle and B. Webb, "Air jet impingement heat transfer at low nozzle-plate spacings," *International Journal of Heat and Mass Transfer*, vol. 37, no. 12, pp. 1687–1697, 1994.

[45] K. Nishino, M. Samada, K. Kasuya, and K. Torii, "Turbulence statistics in the stagnation region of an axisymmetric impinging jet flow," *International Journal of Heat and Fluid Flow*, vol. 17, no. 3, pp. 193–201, 1996.

[46] S. Satake and T. Kunugi, "Direct numerical simulation of an impinging jet into parallel disks," *International Journal of Numerical Methods for Heat & Fluid Flow*, vol. 8, no. 7, pp. 768–780, 1998.

[47] S.-J. Lee, Jungho Lee, "Stagnation region heat transfer of a turbulent axisymmetric jet impingement," *Experimental Heat Transfer*, vol. 12, no. 2, pp. 137–156, 1999.

[48] H. Jasak and H. Rusche, "Dynamic mesh handling in openfoam," in *Proceeding of the 47th Aerospace Sciences Meeting Including the New Horizons Forum and Aerospace Exposition, Orlando, FL*, 2009.